Frontiers of Cancer Diagnostics: From Photoacoustic Chemical Imaging to Cellular Morphodynamics

by

Jeff Folz

A dissertation submitted in partial fulfillment
of the requirements for the degree of
Doctor of Philosophy
(Biophysics)
in The University of Michigan
2020

Doctoral Committee:

Professor Raoul Kopelman, Chair
Professor Ari Gafni
Professor Danai Koutra
Professor Xueding Wang
Professor Kevin Wood

Jeff Folz

folzja@umich.edu

ORCID iD: 0000-0002-4823-3343

TABLE OF CONTENTS

LIST OF TABLES

Table

LIST OF FIGURES

Figure

ABSTRACT

While terrific progress has been made over the last century, cancer continues to be a prevalent, lethal disease and is responsible for millions of deaths each year. The advent of personalized medicine has brought great strides in the treatment of cancer, as clinicians are able to select therapeutic courses that have been tailored to patients specific set of biomarkers. This selection, in principal, maximizes the chances of cancer remission while minimizing overall patient harm. In this spirit, we have focused on developing diagnostic techniques for two separate cancer biomarkers: tumor potassium concentration, and cell morphology.

We first developed an ionophore-based potassium sensing nanoparticle. The sensor works on the principle of Donnan exclusion in which the overall charge of the carrier remains constant. The hydrophobic interior of the nanoparticle holds a pH-sensitive dye and a potassium ionophore. As the potassium concentrations rise, the ionophore chelates potassium from the solution which results in a proton being removed from the pH dye to maintain charge neutrality. The deprotonation event can be calibrated for quantitative measurement and this sensor was developed for use in diverse imaging modes, which include UV-VIS absorption, fluorescence, and photoacoustics. At physiological pH and in the presence of interfering ions, we were able to quantitatively measure potassium concentrations using each of these readouts.

We modified the potassium sensor to enable *in vivo* measurements of potassium. This formulation makes use of a solvatochromic dye that transitions from the par-

ticle's interior to its surface as potassium is chelated, and thus avoids inherent pH-cross sensitivity. Using photoacoustic chemical imaging, we are able to quantitatively measure the potassium concentration in the tumor microenvironment. As predicted, it was shown that the TME is hyperkalemic, having a potassium concentration of 29mM. The results of the *in vivo* photoacoustic analysis were verified with ICP-MS measurements of TME potassium.

Finally, we combined cell magneto-rotation and machine learning to develop a technique to measure the metastatic potential of a cancer cell population. This technique aims at avoiding the use of expensive and difficult to produce biological labels. By magnetically activating cells, we are able to suspend them in an oscillating magnetic field where they are free to explore their morphological shape space. By collecting fluorescence images of these cells, we are able to train a classifier to recognize cells of a given type. A proof of concept for the technique is provided here, where MCF-7 and MDA-MB-231 cells, both breast cancer but of different metastatic potential, were classified. A random forest classifier trained on cell images was able to correctly identify the cell type with 86.9% accuracy.

CHAPTER I

Introduction

Nanoparticles (NPs) offer an attractive avenue for both therapy and diagnosis of cancer. NPs are capable of shielding sensitive molecules from premature degradation and can act as carriers of drugs or contrast agents whose solubility may otherwise prevent their administration. NPs benefit from both passive and active targeting to the tumor area. Therapeutics are then able to release their payloads with minimal interaction with healthy tissues while diagnostics particles can provide contrast for imaging and other chemical information about the tumor and its environment.

1.1 Journey to the Tumor Microenvironment

Many therapeutics are administered intravenously, and direct injection of therapeutic or diagnostics agents is avoided due to the invasive nature of the procedure. Upon entering the bloodstream, the agents are delivered to the tumor via small blood vessels, especially capillaries [42]. Healthy capillaries are tightly sealed by a layer of endothelial cells, which themselves are firmly attached to pericytes anchored in a relatively thick (100-150nm) basement membrane [2, 120, 67]. To travel from the blood stream to a target organ, an agent must pass through each of these layers. Accumulation in the tumor area is aided by abundant neovasculature. Unlike healthy blood vessels, these tumor vasculatures have large pore openings (0.1-0.3um), which

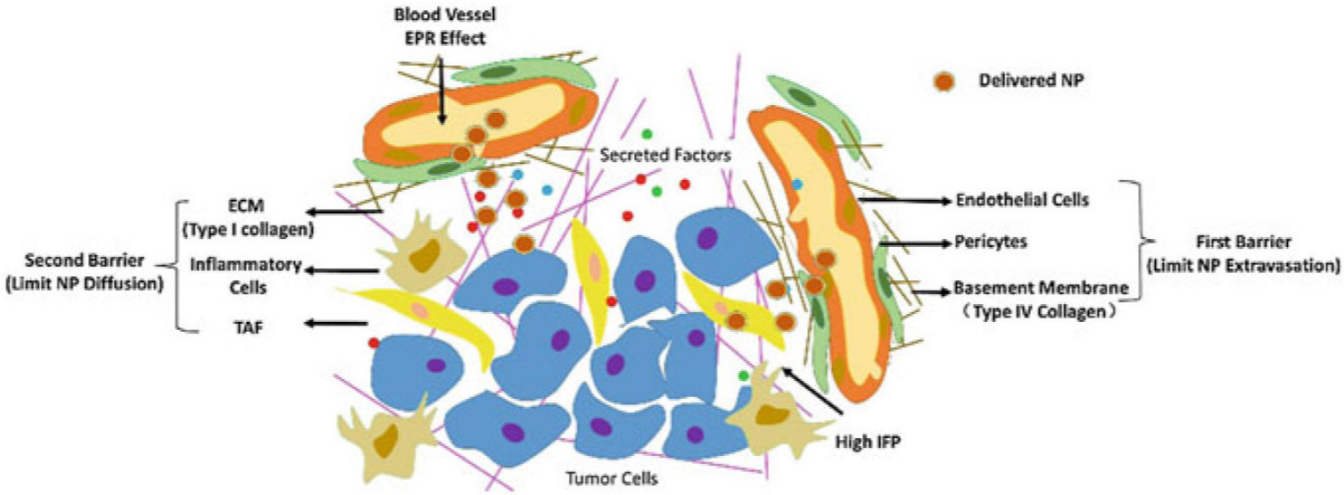

Figure 1.1: A schematic summary of the tumor microenvironment. NPs delivered from the blood stream must extravasate through the epithelial walls, pericytes, and basement membrane. Next, diffusion guides the NPs to the tumor parenchyma, which itself acts a barrier as the collagen, immune cells, and fibroblasts (TAFs) inhibit NP diffusion [70].

leads to increased permeability and hydraulic conductivity [89, 23]. The extent of pericyte coverage in neovasculature is diminished relative to healthy tissues [2]. Further, both these pericytes and the basement membrane have only a loose connection with the endothelial vasculature and penetrate into the tumor tissue [81, 2, 103, 105]. These leaky, porous openings - coupled with dysfunctional lymph vessels - produce the *Enhanced Permeability and Retention Effect*, which promotes nanoparticle accumulation in the tumor area.

To exit the bloodstream, nanoparticles must pass through the endothelial cells of the blood vessel, but also the smooth muscle cells lining the vessel and the associated basement membrane. The endothelial cells present minimal challenge, as the gaps between cells allow for NPs as large as 100nm to pass through. Though far less rapid, active endocytosis of epithelial cells on the distal (blood) side of the vessel and exocytosis on the proximal (tumor) side can also lead to accumulation of particles in the TME. Associated with the endothelial cells of the blood stream are two additional components that affect delivery: pericytes and the basement membrane. Pericytes

are a common feature of the TME; they are the smooth muscle cells that wrap around blood vessels [2, 21].

Pericyte coverage can both inhibit and promote nanoparticle extravasation. Pericyte coverage varies among tumor types, and can even be heterogeneous within a single tumor [2, 71, 91]. By ablating pericytes, vascular tortuosity is increased, as does tumor growth [79, 64]. Naively, this ablative approach would be beneficial to treatment, as it would promote nanoparticle or therapeutic extravasation. Indeed, inhibition of pericyte formation was shown to increase the intratumoral penetration of sub-100nm nanoparticles [91, 41]. However, this outcome was only achieved in a tumor model with high pericyte coverage (70%). Paradoxically, tumor models with low pericyte coverage also display resistance to extravasation due to the inhibition of vessel function. Here, it is actually through the promotion of pericyte recruitment and subsequent vascular normalization that nanoparticle penetration is improved [92, 144]. Thus, when considering delivery, neither high nor low pericyte coverage can be considered as ideal.

The basement membrane (BM) is a thin layer of extra-cellular matrix that surrounds blood vessels. In healthy tissue, 99% of vasculature is surrounded by an approximately 100nm thick BM [103]. However, in tumors, the BM can take many forms, and be either loosely or strongly associated with vasculature. The collagen layers of the BM act as sieve, and restrict passive diffusion. The thicker the collagen layers, the "finer" the BM sieve will be. Typically, the BM restricts diffusion of particles greater than 100nm, but as additional layers of collagen build-up, passive diffusion is increasingly attenuated.

A final factor for NP extravasation to consider is interstitial fluid pressure (IFP). In normal tissues, IFP is roughly 0mm Hg, whereas tumors have an IFP comparable

to that of blood vessels themselves (10-40mm Hg) [84]. This increase in pressure is caused by the disruption to the lymph vessels in the tumor area. As lymph vessels are responsible for draining excess blood, proteins, and fluid from the TME, their disruption results in stagnation and IFP increase. This inhibits fluid exchange in tumor-associated capillaries and promotes passive diffusion into the tumor, which is a much slower process than convection, especially for larger particles [118, 157]. The increased pressure can further induce tumor stroma into squeezing the microvessels, resulting even greater restriction of blood flow [138] and the formation of stagnant pockets that are cut off from circulation.

Having traveled through the bloodstream to the tumor, extravasated, and progressed through the basement membrane, the nanoparticle finally arrives in the tumor interstitium. However, despite having arrived at the target destination, the problems of delivery have not fully abated.

Diffusion through the tumor interstitium is principally governed by the abundance of collagen ECM, which is heterogeneous within a single tumor and among tumor types[118, 31, 38]. Tumors with little ECM, such as melanomas, allow for quick, passive diffusion of nanoparticles through the tumor. However, passive diffusion becomes intractable as collagen density increases. Further, as tumors mature, the collagen fibers thicken and align, which narrows the interfiber spacing and further impedes nanoparticle diffusion [78]. This process also leads to directed diffusion, or diffusion anisotropy [136]. While the collagen acts as a physical barrier, preventing NP diffusion, the collagen-associated proteins and sugars, particularly glycosaminoglycans, can also inhibit particle diffusion via electrostatic interactions [83, 98]. NPs are typically strongly charged to prevent aggregation. Glycosaminoglycans are highly negatively charged, and will non-specifically bind positively charged materials.

1.2 The Therapy Resistance Triad

The tumor microenvironment (TME) is a complex milieu of small molecules, structural proteins, native cell types, and cancerous cells. Traditionally, the relationship between cancer cells and this environment has been neglected, and a one-size-fits all approach has been adopted for the administration of therapeutics. However, the TME can have significant influence on the efficacy of treatment. Dubbed the "therapy resistance triad" oxygen, pH, and potassium each exhibit profound attenuating effects for various forms of treatment. Thus, the ability to measure these parameters, and therefore choose a therapeutic course whose viability is not inhibited by the TME's composition, could be of significant diagnostic benefit.

The best known of the therapy resistance triad is oxygen. It has been known for over a century that oxygen concentrations in the tumor area are depleted [101]. Radiation therapy, whether x-ray or gamma, exerts its effect by ionizing oxygen in a solution [123, 72, 90]. It is through the creation of reactive oxygen species, and their associated deleterious effect, that radiation therapy exerts its therapeutic effect. Thus, without sufficient oxygen concentration, radiation therapy becomes a non-viable avenue of treatment. While it is most strongly attenuating for radiation therapy, the hypoxic environment exerts effects on both chemo- and immune therapy as well. Hypoxia is an inhibitor of many chemotherapeutic drugs, including vincristine [15, 16], melphalan [124], methotrexate [10], and cisplatin [12]. Further, low oxygen environments have been shown to affect cells of both the adaptive and innate immune system [63, 115, 96, 132].

Even in the presence of sufficient oxygen, therapy can run afoul. The Warburg Effect manifests as a preference for anaerobic glycolysis observed in cancer cells even

in the presence of sufficient oxygen. It is hypothesized that avoiding oxidative phosphorylation and the associated ATP production allows promoting anabolic activity and the formation of biomass [69]. A side effect of this metabolic aberration is the accumulation of lactic acid in the cytosol and its subsequent exportation to the TME, leading to acidosis [80]. As many chemotherapeutic drugs are weakly basic, the acidic environment induces protonation, preventing their passive diffusion across the plasma membrane. Affected drugs include paclitaxel, vincristine, and vinblastine [100, 50, 73]. Acidosis further impedes immune [122, 142] and radiation therapy [50, 55].

The final member of the therapy resistance triad is potassium. It is worth going into detail regarding the relationship between immunotherapy and potassium as it pertains to the TME. Cells in the TME are forced to compete fiercely for resources which leads to clumps of cells without access to sufficient resources and nutrients [45, 127]. These areas often develop into dense areas of cellular apoptosis and necrosis [117]. These apoptotic and necrotic regions alter the extracellular milieu due to the release of dying cells' intracellular contents, and notably, ions [162, 87]. It is well known that T cells present in the tumor microenvironment retain their response to tumor-associated antigens [139], but their function is heavily suppressed in the TME [85]. Further, intact ion transport is critical to T cell function, as disruptions to both calcium and magnesium channels result in severe combined immunodeficiency in humans [139, 32, 102]. These observations lead Eil and colleagues to hypothesize that perturbations to ion concentrations in the TME lead to the inhibition of immune cells. In two seminal papers, elevated extracellular potassium resulted in profound disruption to T cell function.

Eil and colleagues showed that necrosis in the tumor microenvironment lead to

a 5-10 fold increase in the local potassium concentration, though they observed no change for other ions (sodium, magnesium, calcium, and chloride). Elevated extracellular potassium resulted in a steep decline of T-cell receptor induced cytokine production. Eil further determined that the reduction of cytokine production was due to the hypophosphorylation of PP2A. Thus, elevated extracellular potassium lead to disruptions in the signal transduction of the T cell receptor, preventing any effector function to manifest itself in the T cells' epigenetics [29]. In a follow-up study, Eil and colleagues demonstrated that elevations in potassium disrupted the nutrient transport in T cells, resulting in autophagy and the inability to mature. These "starved" T cells displayed a marked increase in *in vivo* persistence, clonal renewal, and multipotency, matching the characteristics previously observed in tumor-associated T cells [37, 36]. Finally, it was demonstrated that T cell function could be rescued by the depletion of intracellular potassium [143].

1.3 Photoacoustic Chemical Imaging

Photoacoustic imaging (PAI) is an imaging modality that combines the *in vivo* penetration depth of ultrasound with the contrast of standard optical techniques [22, 141, 147]. For simplicity, PAI can be broken down into three critical steps: the absorption of a photon, thermal dissipation of the absorbed energy, and the subsequent propagation of an ultrasonic wave [14]. First, a non-ionizing input beam excites a target molecule. This excitation can be dissipated via radiative decay or thermalization. In PA, thermalization is preferred as radiative decay (fluorescence, phosphorescence) is strongly scattered; it often cannot be detected, and no image can be reconstructed. Thus the relaxation from the excited state to the ground state is the second critical step in PAI. Here, optical energy is converted to ultrasound

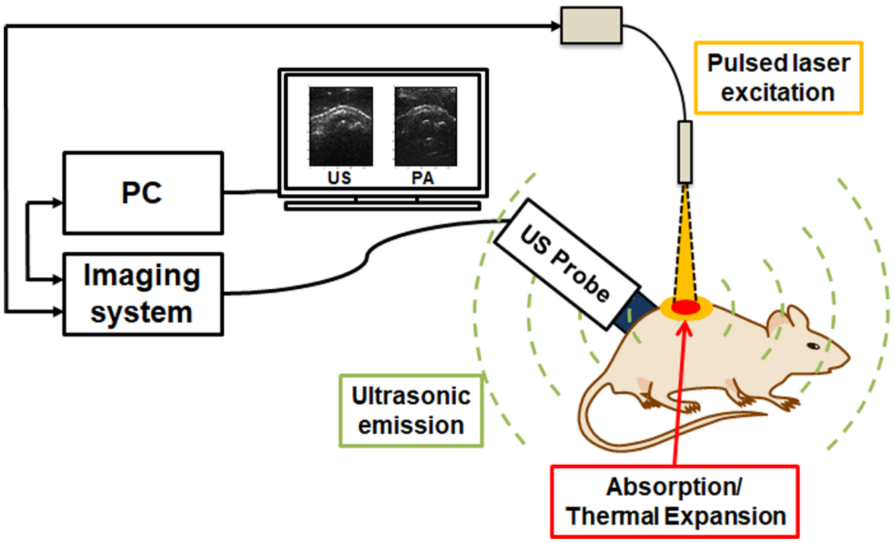

Figure 1.2: A visual summary of photoacoustic imaging. First, a pulsed laser excitation results in absorption and thermalization at the location of interest, which take many forms, such as a sample tumor on a mouse, or a tube containing solutions for *in vitro* measurement. The thermalization produces an ultrasound wave which can be detected by an ultrasound transducer. An image of the targeted area can then be reconstructed.

as vibrational and collisional relaxation results in local thermalization. The small increase in local temperature is accompanied by an increase in local pressure. It is this pressure increase that causes a propagating acoustic wave due to the elastic nature of tissue. This ultrasonic wave is then measured via an ultrasonic transducer and an image can be reconstructed (Figure 2).

Photoacoustics has seen tremendous development over the previous decade and a half. *In vivo* functional PAI was first reported for mapping rat brain structures and hemodynamic changes in response to whisker stimulation [151]. PAI has been applied to imaging angiogenesis, blood oxygenation, cerebovascular activity [126, 116, 54]. One principal advantage of PAI is that we may use either endogenous or exogenous chromophores when performing measurements. While blood is the dominant chromophore in the body, exogenous contrast agents can be used in PAI. These exogenous agents can provide more than just contrast, however. If the dye

in question is sensitive to particular analyte, than photoacoustic chemical imaging can be performed, in which each pixel of the PA image gives structural as well as chemical information, allowing for *photoacoustic chemical imaging* [20]. Two major examples of such an approach are oxygen and pH.

If PAI can be used to measure blood oxygenation, it is natural to wonder what the purpose of an exogenous PA oxygen sensor is. The subtle distinction between the two arises in measuring blood oxygenation versus tissue oxygenation. Blood oxygenation pertains to the relative amount of oxygenated hemoglobin to the total hemoglobin concentration whereas tissue oxygenation refers to unbound molecular oxygen in solution [107]. To measure tissue oxygenation with PACI, photoacoustic lifetime imaging is coupled with an oxygen sensitive dye, such as G2 oxyphor [7, 135]. A pump laser excites the G2 dye into an excited triplet state. The lifetime of the excited state for G2 is sensitive to the oxygen concentration of the solution. Using a probe laser, the phosphorescent decay of the excited state is measured, and the decay rate is correlated to a particular saturation of oxygen. Using this approach, oxygen concentrations were quantitatively measured *in vivo* with a mouse model [51, 108].

pH is a second analyte that has been measured using PACI. Initial attempts to measure pH were done *in vitro* using buffer solutions contain the radiometric pH indicator SNARF-5F. By exciting the dye at its isosbestic point, 532nm, and its sensing point, 564nm, the ratio of the photoacoustic signals' intensity at those two excitation wavelengths was able to be calibrated against a pH gradient [137]. This method was further improved by encapsulating SNARF-5F in a polyacrylamide hydrogel nanoparticle, which allowed for active targeting and protected SNARF-5F from adsorption by albumins, which significantly impacted its sensitivity [8]. *in*

vivo imaging and pH measurements were accomplished on a rat joint model with resolution below 0.1 pH units.

Another approach to PA pH measurement approach the use of a DNA triplex [68]. This active DNA structure operates through a principal analogous to FRET, though the signal modulated is PA intensity rather than fluorescence intensity. At high pH (8.0), the complex is disorganized, and the strands of the 3 ends do not interact significantly. As the pH drops over the physiologically relevant range of 6.0 to 8.0, the DNA complex becomes increasingly ordered and the probe begins to fold onto itself, bringing the 3' ends into tighter proximity. As such, the excited fluorescent probe begins to be actively quenched, and the photoacoustic signal increases. While this sensor is quite novel, it has not yet been demonstrated *in vivo*.

In vivo PACI of pH was achieved through the use of an exogenous dye [8, 52]. SNARF-5F - a pH-sensitive dye - was embedded in a polyacrylamide hydrogel matrix that was actively targeted to the tumor area using F3. The absorption spectrum of SNARF-5F changes as a function of pH, with the dye's pK_a being approximately 7.2, which is well-suited for the expected biological range. In an optical setting, the two absorption peaks of SNARF-5F can be simultaneously imaged or excited to obtain a ratiometric pH measurement that is independent of dye concentration. A similar approach is taken in the photoacoustic setting, but both deoxy- and -oxygenated hemoglobin must be taken into account. To do so, the photoacoustic signal, which is directly proportional to the overall absorption, is modeled as the linear sum of signals from the independent absorbers.

$$PA_\lambda = k(\varepsilon^\lambda_{Hb}[Hb] + \varepsilon^\lambda_{HbO_2}[HbO_2] + \varepsilon^\lambda_{NP}[NP]) \tag{1.1}$$

Using this approach, the pH of mouse model tumors was measured, and found to

be approximately 6.7 [52]. The acidic environment of the tumor was expected [80]. When measurements were done in healthy tissue, the pH was found to be 7.46.

1.4 Ionophore-based Optical Sensors

Ionophore-based optical sensors are now over 25 years old, and their first reports are on bulk optodes [134, 121]. These optodes (optical electrodes) were essentially miniaturized versions of ion-selective electrodes. Sub-micrometer sensors were achieved in the Kopelman lab by photopolymerizing a pH-sensitive dye in an acrylamide membrane on a fiber optic tip [146]. Miniaturization was further extended by encapsulating sensors in miniaturized micro- or nanosphere carriers with hydrophobic cores. Ionophore-based optical sensors operate on the principal of Donnan exclusion wherein the hydrophobic core of the sensor must remain electrically neutral. Figure 3 shows a typical sensing mechanism where three components work in harmony to measure a cation, such as potassium. At low analyte concentrations, the pH dye is fully protonated; the proton lends the dye a positive charge. These positive charges are balanced by anionic sites that are added to the nanoparticle; they have no significant role beyond imposing electric neutrality. The final component is the ionophore. Its role is to selectively chelate the analyte of interest from solution, such as potassium. Once bound, the cation lends its positive charge to the ionophore, leading to an overall charge imbalance. To correct for this imbalance, the chromoionophore loses a proton. The deprotonation event causes a shift in the dye's absorption spectrum which can be calibrated for quantitative analysis.

A major advantage of these sensors is their generalization. Simply switching ionophores renders a sensor responsive to another ionic analyte. Thus, ion-selective sensors have been made for sodium [112, 56, 57, 141, 154, 77, 82] potassium [93,

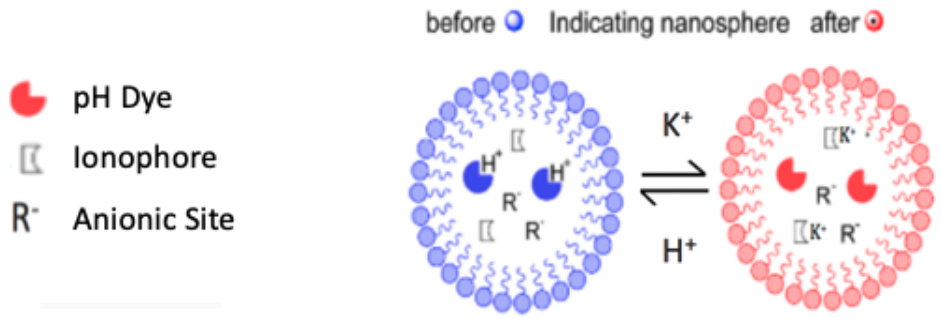

Figure 1.3: A schematic representation of an ionophore-based optical sensor's function. On the left, we see that the pH dye (chromoionophore) is fully protonated. As the potassium concentration increases, the pH dye loses a proton and changes color as the ionophore chelates potassium from the solution phase.

156, 140], calcium [22, 153], chloride [86, 130], zinc [59], magnesium [30], iron [58], and lithium [61] among others. One of the principal advantages of these optodes is their specificity. The ionophores are highly specific to the ion of interest, and their selectivity is preserved similar across different films and environments [48, 111]. The overall dynamic range and sensitivity of these sensors can be adjusted by changing the ratios of the three sensing components in the initial preparation. Ultimately, however, the sensing range and specificity are governed by the binding constants of the two exchangers. For example, a pH dye with an extraordinarily strong affinity for protons would require a far higher concentration of analyte to force a deprotonation event than would be required for a chromoionophore with weak affinity.

Careful selections must be made beyond the sensing components, however. The platform (carrier) can have a marked impact on a sensor's capabilities. Ionic components can prevent exchange of ions, or even exhibit weak chelation of ions. A second aspect of the sensors is the requirement of the carrier to be in a rubber-like versus a glassy phase [150]. The phase of a sensor is described by its glass transition temperature, below which amorphous solids will enter a fixed, glassy state. The glassy state strongly inhibits ionophore exchange and prevents sensor function. The choice

of plasticizer is not necessarily simple either, as it can influence the selectivity of a carrier towards divalent or monovalent ions [150, 26].

CHAPTER II

An Ion-Selective Nanosensor for Photoacoustic and Fluorescence Imaging of Potassium

This chapter has been adapted from the following publication to add additional data and emphasize personal contributions:

Lee CH, **Folz J**, Zhang W, Jo J, Tan WYJ, Wang X, and Kopelman R. "Ion-Selective Nanosensor for Photoacoustic and Fluorescence Imaging of Potassium." *Analytical Chemistry*, **89** (2017), pp 7943-7949.

2.1 Introduction

The analysis of whole body fluids, such as blood, urine, or sweat, is one of the most valuable diagnostic tests available to the modern clinician [26]. Typically, these tests employ a standard ion-selective electrode, whose selectivity for the analyte of interest is exquisite [27, 34, 152]. However, these tests, due to the bulky and invasive nature of electrodes, are often limited to harvested or *ex vivo* samples. To perform *in vivo*, the electrode itself must be minimized, which can be accomplished via fiber optics [146] or through the synthesis of nanoPEBBLEs [131, 40].

Potassium makes an attractive target for such analysis due to its ubiquity, high physiological concentration, and diverse function [9]. Its most famous role is the part it plays in generating nerve impulses, but it also serves physiological roles by

maintaining osmotic pressure and pH balance in the body. In cancer, potassium's accumulation in the tumor microenvironment has been shown to inhibit immune therapy [29, 143]. At a cellular level, potassium efflux has been shown to play a critical role in the activation of the MLRP3 inflammasome [110]. Finally, potassium also plays a critical role in apoptosis, and is considered to be an early marker for cell death [18].

A variety of miniaturized potassium sensors have been produced, though their application *in vivo* has been limited for a variety of reasons. Most sensors are geared toward cellular measurements, and their fluorescent output is difficult or impossible to detect *in vivo* [76, 112, 66]. If sensors are built-on fiber optic or microfluidic platforms, their bulk renders them impossible to apply non-invasively [57, 46, 114, 13]. Still other sensors rely on adjusting pH for having fine control of the measurement [75]. Here, we will focus on developing a potassium sensor for both fluorescence and photoacoustic measurement. Fluorescence allows the sensor to be applied *in vitro* while photoacoustics permits *in vivo* application.

2.2 Methods

2.2.1 Synthesis and Characterization of KNP

KNP are synthesized using a thin film rehydration method. Into 10mL of dichloromethane, dissolve 84mg Pluronic F68, 116mg Pluronic P123, 14μL dioctyl sebacate (DOS), 5μL 1,6-hexanediol dimethacrylate (HDMA), 5μL butyl methacrylate (BMA), 1.5mg chromoionophore 1, 5mg potassium ionophore 3 (BME-44), and 9.75mg sodium tetrakis[3,5-bis-(trifluoromethyl) phenyl]borate (NaTFPB). To produce a thin film, the solvent is then rotoevaporated. The thin film is left to dry overnight, and rehydrated then next day by adding 10mL of millipore water and stirring with a magnetic stir bar. The solution is flushed with argon and kept un-

der an inert atmosphere. After 20 minutes of flushing with argon, add 100μL of N,N,N',N'-tetramethyl ethylenediamine followed by 100μL of a 10% (w/v) ammonium persulfate to induce radical polymerization. After 2 hours, the flask is uncapped to quench the reaction. The particles are washed using an Amicon Ultra-15 Centrifugal Filter (100kDa) with water until the solution turns blue.

KNPs were characterized at concentration of 1mg/mL. Dynamic Light Scattering and zeta-potential measurements were performed with Beckman Coulter zeta-analyzer Figure Figure 2.1. Absorption spectra were collected using a UV-VIS spectrophotometer (Shimadzu UV-1601), fluorescence spectra a fluorimeter (Horiba FluoroMax-3). All measurements were done in Mops-buffered saline solution (MBS).

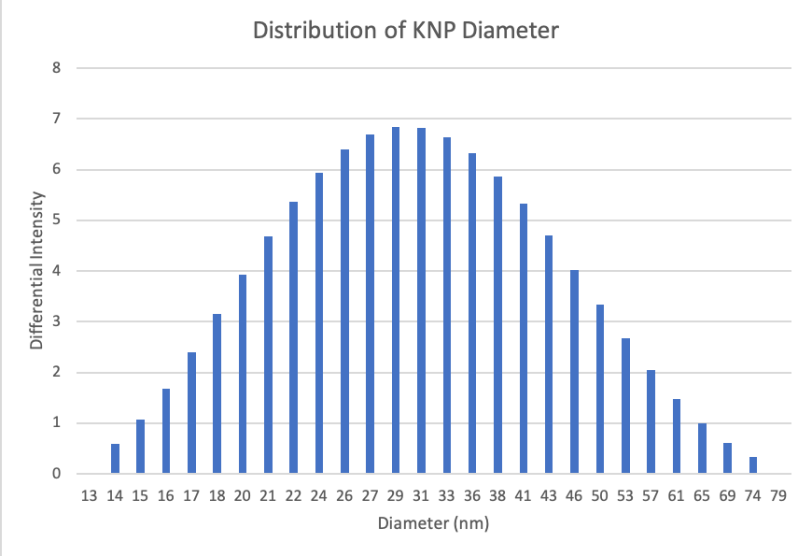

Figure 2.1: Dynamic Light Scattering analysis of the KNP's diameter. The polydispersity index was 0.28 and 90% of particles had a diameter of 47.8nm or below. Data was collected at a particle concentration of 1mg/mL.

The calibrations conducted at various temperatures used the heating attachment of the Shimadzu 1601. Solutions were prepared and a calibration curve was gathered at room temperature. The solutions were then individually heated, and their spectra measured. All solutions were given 30 minutes to cool before the final spectra were

collected.

2.2.2 PA Spectroscopy Setup

An optically clear polyvinyl chloride tube (I.D. x O.D. = 1/16 in. x 1/8 in.), containing solutions of the KNP (5 mg/mL), with various concentrations of K^+, was placed in a water bath. An optical parametric oscillator (SLOPO Plus, Continuum), pumped with the second harmonic of a pulsed (5 ns) neodymium-doped aluminum garnet (Nd: YAG) laser (Surelite, Continuum), was used for excitation (at 540 and 660nm wavelengths, respectively). The PA signal was detected by a 2.25 MHz unfocused ultrasonic transducer (V323, Panametrics) connected to an amplifier (5072PR, Olympus). The signal, digitalized by an oscilloscope (TDS540, Tektronix), was collected (averaged over 200 pulses). The laser pulse was focused with a converging lens where the sample is located inside the tube. The raw PA signals are normalized with the power of the laser and PA signals from the empty tube. The signal intensity at 540nm when divided by the signal intensity at 660nm gave the ratio used for calibration. With ratios determined for each sample at each potassium concentration (n = 4), an average and a standard deviation were obtained.

2.2.3 Photoacoustic Imaging Setup

Gelatin phantoms were prepared by dissolving gelatin (from porcine skin) in hot water (80g/L) containing 16 gauge needles. Then, the phantom cooled down to room temperature overnight. The 16 gauge needles were carefully removed and four different solutions of KNP at 5mg/mL were added. As soon as the solutions were inserted, the PA images were acquired by an imaging system built on commercially available research (V1, Verasonics) with a linear array probe (CL15-7 with a central frequency 11.25MHz, Philips) working at 10Hz. The laser pulse was diverged with a

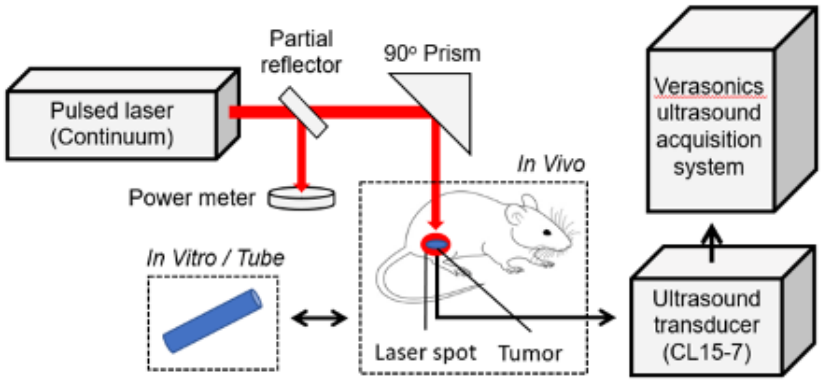

Figure 2.2: A schematic illustration of the photoacoustic spectroscopy and imaging set-up. A laser is focused on a region of interest, which could be either a tube or mouse tissue. The pulsed excitation light induces local thermalization at the region of interest. The ultrasound output of the thermalization, expansion, and retraction process is detected by an ultrasound transducer. An image of the targeted area can then be reconstructed.

diverging lens so as to cover the entire imaging region (1.5 cm x 3 cm). The phantom PA images (540nm and 660nm) were averaged over 50 images and were smoothed by a Gaussian filter. The phantom PA image at 540nm was divided by the phantom PA image at 660nm so as to acquire the ratiometric potassium image.

2.2.4 Cell Imaging and Assays

HeLa cells were grown in DMEM supplemented with 10% fetal bovine serum and 1% penicillin-streptomycin.

For the MTT assay, 25,000 cells were plated in each well on a 24-well plate. Cells were allowed to grow 1 day after deposition after which they were incubated with the KNP at 200μg/mL for 24 hours. Following incubation, the media was removed and replaced with 5mg/mL MTT reagent in PBS. The cells were further incubated for 4 hours, after which the MTT solution was replaced with DMSO. After 1 hour additional incubation, the DMSO solutions were removed and read with UV-VIS spectrophotometer. Trials were repeated in groups of 4.

For confocal imaging, 100,000 HeLa cells were deposited on a confocal microscopy

plate. After 1 day of growth, cells were incubated with 50nM lysotracker green. After 90 minutes, 1mg/mL KNP was added to the solution. After 30 minutes incubation, the media was removed, the plate washed several times, and replaced with transparent media.

2.2.5 Degree of Protonation Calculations

Calibrations are typically given as the protonation degree as a function analyte concentration. In a sensing-system with two separate sensing peaks, such as the KNP, we calculate the protonation degree from the raw spectra as shown in equation 2.1:

$$\pi = 1 - (1 + S\frac{R - R_{min}}{R_{max} - R})^{-1} \tag{2.1}$$

where S is the scaling factor, defined as $A^{max}_{540nm}/A^{min}_{540nm}$, R is A_{660nm}/A_{540nm}, R_{max} is $A^{max}_{660nm}/A^{min}_{540nm}$, and R_{min} as $A^{min}_{660nm}/A^{max}_{540nm}$. Here, A denotes the absorption at a particular wavelength from the raw spectrum (see Figure 2.3); 'min' and 'max' refer to the smallest and largest absorption values obtained at that wavelength.

2.3 Results

The KNP consists of three sensing components encapsulated in a combination Pluronic F68 and Pluronic P123 micelle. The core of the micelle contains three additional components: DOS, HDMA, and BMA. The latter two, HDMA and BMA, are hydrophobic monomers that are polymerized to give the core of the KNP more stability and to help prevent spontaneous micelle disassembly. DOS is a plasticizer, so its role is to decrease the glass transition temperature of the two Pluronic polymers. The raw spectrum of the KNP at various potassium concentrations, as well as a calibration curve, can be seen in Figure 2.3.

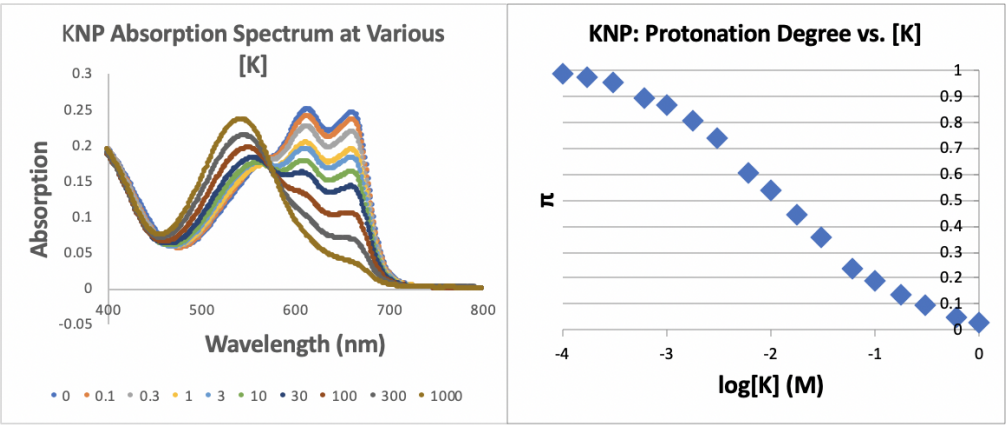

Figure 2.3: Left) Raw UV-VIS absorption spectra for the KNP at 1mg/mL. Potassium concentrations (mM) are indicated by the legend. The protonated peak is 660nm while the deprotonated peak is 540nm. Right) A simple calibration curve for the KNP, where π is the fraction of protonated chromoionophores. Note that the x-axis is the log of the potassium concentration.

The raw spectra of the KNP demonstrates two peaks: a protonated peak at 660nm and a deprotonated peak at 540nm (Figure 2.3, left). The protonated peak decreases with increasing concentration of potassium. The right figure in 2.3 shows a calibration curve for the KNP. The y-axis, π, is the degree of protonation for the chromoionophore, and is equivalent to the fraction of protonated dyes relative to the total dye concentration. Thus, the protonation degree is initially 1, as all the dyes are protonated. As the potassium concentration increases, the sigmoidal response curve enters its linear region, and we can see a semi-linear response between 1-300mM, which covers the relevant physiological concentrations of potassium. Beyond 300mM, the sensor is beginning to become saturated with potassium and very few dyes remain to be deprotonated.

A fluorescence calibration curve was collected for the KNP, shown in Figure 2.4. We chose to excite the KNP at 540nm, as the deprotonation peak increases with the analyte of interest. The emission peak of the KNP is at 680nm. To perform quantitative measurements, we attached a reference dye, NIR797. The secondary

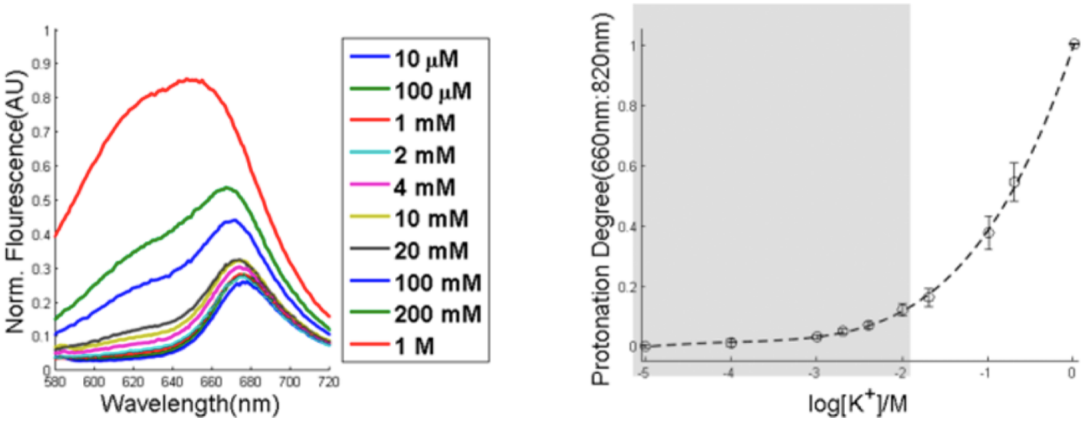

Figure 2.4: Left) Fluorescence emission spectra of 1mg/mL KNP with a 540nm excitation. The 540nm absorption peak is selected as its absorption increases with potassium concentration. Right) A fluorescence calibration curve for the KNP. The sensor is optimized for intracellular fluorescence measurements.

reference dye allows us to perform ratiometric measurements, which do not depend on the concentration of the KNP. This approach is critical for *in vitro* measurements, as simple changes intensity can be attributed to changes in either analyte or dye concentration. The calibration curve shows that the KNP's fluorescence is most sensitive around 100mM K^+, which is ideal for intracellular potassium measurements.

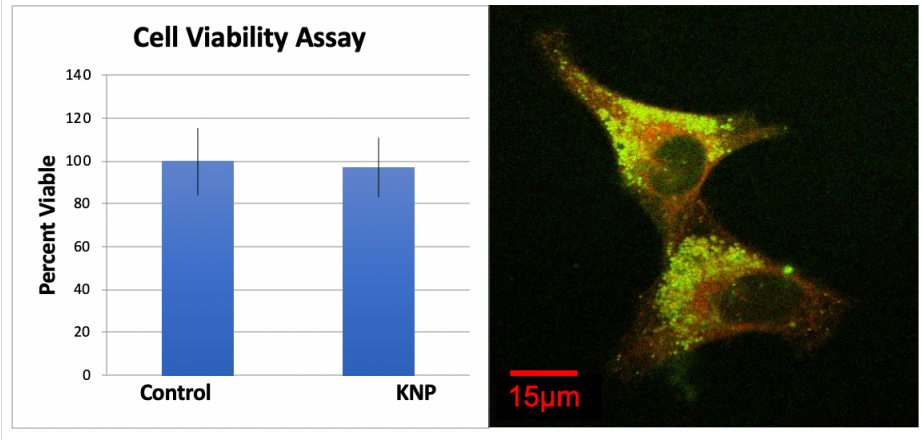

Figure 2.5: Left) An MTT assay performed using the KNP at 200μg/mL. The KNP was incubated with HELA cells for 24 hours. Cell viability was determined to be unaffected by KNP. Right) A close up image of cells incubated with KNP (red) and lysotracker (green). The red haze in the cytosol indicates that the KNP is escaping the endosome. Very few yellow pixels are present, which indicates few KNPs become trapped in the lysosome.

Prior to performing *in vitro* studies, it is critical to make sure that the "ruler", in this case the KNP, is non-toxic. Figure 2.5 shows the results of an MTT assay in which HELA cells were incubated with 1mg/mL KNP for 24 hours. Little toxicity to cells is indicated during that time, as survival rates between the control (no KNP) and the test cells are within error of each other.

Knowing that the particle was not toxic, we also wanted to be sure that any measurements made on the cell were made in the cytosol. The cell is highly compartmentalized, and it is most probable that our particles enter via non-specific endocytosis. If the particles become trapped in the endosomes or lysosomes, it will not be possible to make accurate measurements of the intracellular potassium concentration. Figure 2.5 shows an image of two cells taken on a confocal microscope. The red is the KNP while the green puncta arise from the dye, lysotracker. The KNPs appear as a haze throughout the cytosol, suggesting that they have successfully escaped the endosome. The lysotracker clearly displays puncta, as one would expect to see if they dye were tracking individual vesicles. The dirth of yellow pixels, which indicate the presence of both KNP and lysotracker, suggests that very few individual particles are becoming trapped in lysosomes.

One concern with using the KNP in a photoacoustic regime is that the heat generated by, and necessary for, photoacoustic measurement might alter the KNP's response to potassium. The sensor itself is indirectly sensitive to temperature due to its dependence on a low glass transition temperature. Additionally, the sensor functions at equilibrium with its environment; the equilibrium of a reaction is notably dependent on temperature. To test the KNP's temperature dependence, we took 3 consecutive calibration curves: first at room temperature, then at 37°C, and a final calibration once the sensor had returned to room temperature. Figure 2.6 shows that

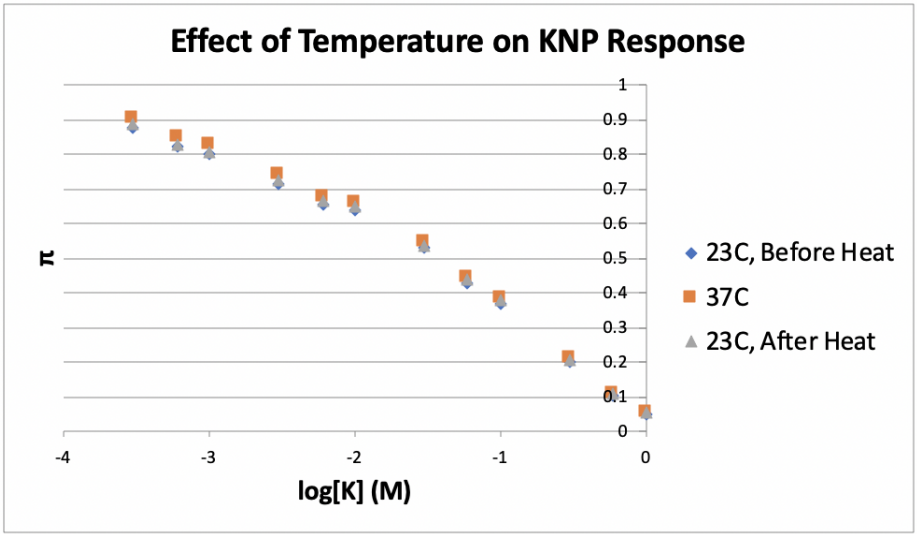

Figure 2.6: A UV-VIS calibration curve of the KNP taken three times in a row at different temperatures. The curve does not shift, which indicates that any heat generated through the photoacoustic effect will not affect the accuracy of the calibration curve.

no temperature sensitivity is observed. Thus, we can be confident that the KNP will produce precise signals in a photoacoustic regime.

The photoacoustic calibration was conducted by placing the the KNP in a gelatin phantom with known concentrations of potassium. Tygon tubing was encased in a gel phantom to authentically mimic *in vivo* photoacoustic image collection. The KNP was excited by a laser at 540nm and 660nm. Figure 2.7 shows that the 540nm signal increases with potassium, while the 660nm signal decreases. This pattern is expected as photoacoustic signal is proportional to absorption and the 540nm absorption peak increases with increasing potassium concentration. The final row of Figure 2.7 shows the ratio of these two measurements, and a clear trend can be seen, especially between the biologically relevant concentrations of 2-100mM.

An inherent disadvantage in using a pH dye as an optical reporter is that the KNP itself becomes cross-sensitive to pH. By definition, if the pH is lower, than the overall concentration of protons is higher. Since the KNP relies on a chemical equilibrium to do its sensing, the excess protons shift the KNP's optical response to

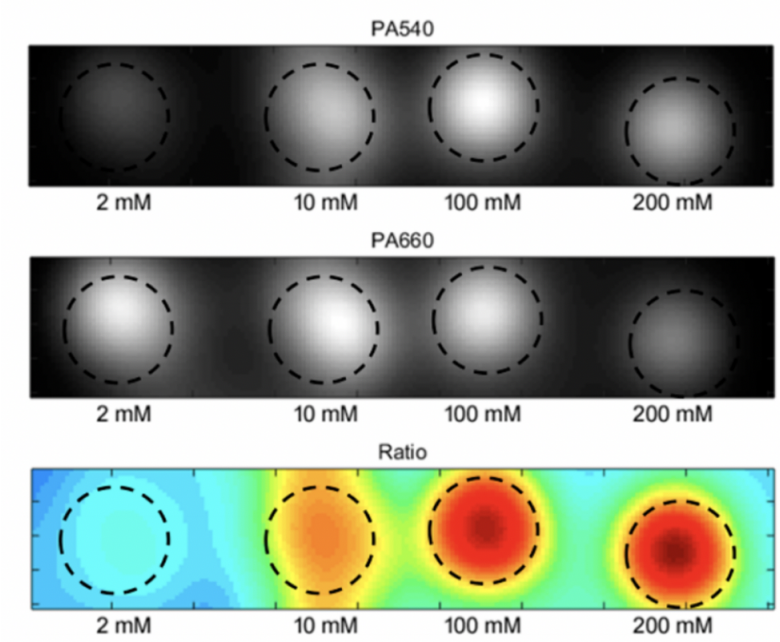

Figure 2.7: A photoacoustic calibration was performed in a gelatin phantom. KNP were placed within a gel phantom at different K^+ concentrations. The KNPs were excited at 540nm (row 1) and 660nm (Row 2) and their photoacoustic outputs were recorded. The third row shows the ratio of the first two. A clear trend can bee seen, as the PA signal increases with potassium.

potassium. At lower pH, a larger potassium concentration is required to induce a deprotonation event. Figure 2.8 shows three calibrations of the KNP, each gathered at a slightly different pH. It is clear that KNP's in a more acidic buffer have a higher degree of protonation for a given concentration of potassium. A large shift in the KNP's response occurs even for a shift in pH smaller than a single unit, and, if uncorrected, could lead to measurements of potassium that are off by more than an order of magnitude.

To overcome this disadvantage, it is necessary to simultaneously measure pH in any environment where the pH cannot be controlled. While most optical experiments can be done in buffers, *in vivo* work precludes such convenience. Thus, we will utilize a pH-sensitive photoacoustic optode [52] to measure the pH of a solution and correct for any shift to the KNP's response. A proof of concept for this approach is provided

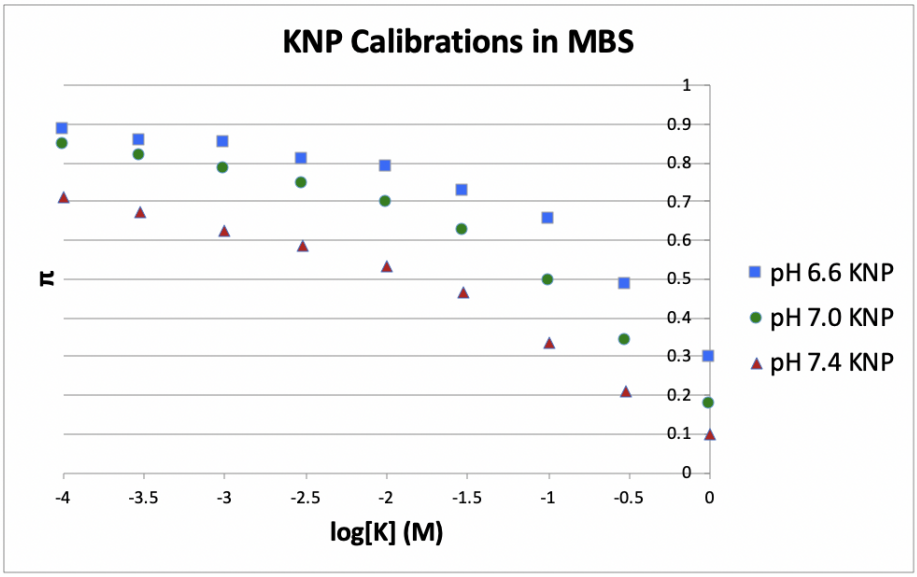

Figure 2.8: Three KNP calibration curves taken at different MBS pH values. The three curves demonstrate the inherent pH cross sensitivity of the KNP.

in Figure 2.9. Figure 2.9 shows three separate potassium measurements each taken at a different pH. There is strong agreement between these calibrations, unlike Figure 2.8. Figure 2.9 shows that we are simultaneously able to measure pH with this approach.

2.4 Discussion

The KNP has been developed for diverse imaging modalities, and thus lends itself to a variety of experiments. As most basic cell work is conducted using fluorescence probes, we ensured that the KNP is capable of quantitative potassium measurement in a fluorescent regime. However, fluorescence is poorly suited for *in vivo* applications. By probing the changes in the KNP's absorption spectrum, we are able to photoacoustically measure the potassium concentration. In all modalities, the KNP is verified to sufficiently cover the relevant physiological potassium concentration range, and it has been verified as minimally toxic.

The KNP itself is easily synthesized, and requires only one pot. The particles are

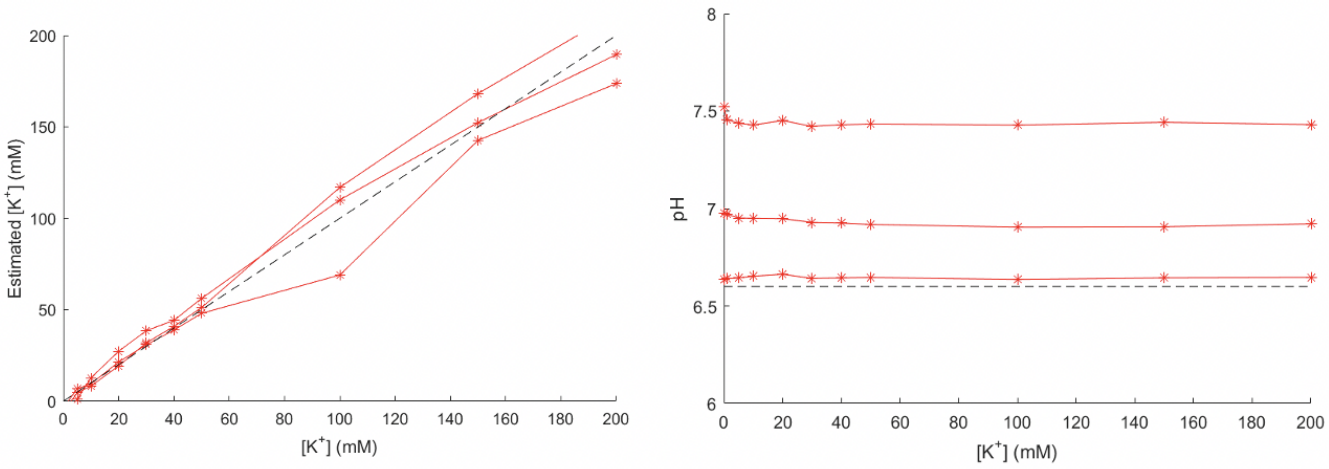

Figure 2.9: Simultaneous measurement of pH and potassium using the KNP and SNARF-5F NP. Three series of potassium calibrations were made in MBS at pH 6.6, 7.0, and 7.4. Through spectral deconvolution, we are able to separate the pH and potassium signals, control for pH, and reproduce quantitative potassium measurements in a manner independent from pH.

readily taken up by cells, and appear to escape from the endosome. By modifying the Pluronic polymer backbone, we can functionalize the KNPs to add reference dyes or targeting moieties [35, 94]. This modification allows for better control of the biodistribution of the KNP, and allows us to preferentially target specific tissues or organelles. Finally, it is worth noting that by swapping the potassium ionophore for another, the platform can be readily adapted for other analytes [158, 27].

The KNP is not without drawbacks, however. The inherent pH cross sensitivity makes it difficult to use in biological settings [34], where the pH is often impossible control without severely disrupting the system of interest. While we have demonstrated that simultaneous measurement of pH can correct for this cross-sensitivity, the implementation and analysis of this approach is far from trivial. Significant spectral overlap exists between the two sensors, especially between the KNP's deprotonated state and SNARF's acidic state. The spectral overlap problem is further exacerbated in the presence of blood. *In vivo*, the process will require measuring

6 different wavelengths at a minimum, two for the analytes, pH and K^+, two for the nanoparticle concentrations for each sensor, and two for oxy- and deoxygnated hemoglobin. Further, each of the selected wavelengths will have different fluence and attenuation effects that must be taken into account to achieve quantitative analysis.

The practicality of using two separate nanosensors is further limited by the realities of biological distribution. As previously noted, biological structures are highly ordered and compartmentalized. To achieve accurate, quantitative potassium measurements, both nanosensors would need to accumulate in the same physiological space. Given that the two sensors have different radii and zeta-potentials, it is not necessarily reasonable to assume that their biodistribution would be identical. If the KNP accumulates in the extracellular space, where the pH is expected be acidic, while the SNARF sensor accumulates in the cytosol, where the pH is expected to be slightly basic, large errors in the potassium measurement would result from an incorrect pH measurement. Thus, even if all of the practical difficulties with the optical set-up and deconvolution were solved, the use of two nanosensors would remain challenging.

CHAPTER III

In Vivo Photoacoustic Potassium Imaging of the Tumor Microenvironment

This chapter has been adapted from the following publication with minimal modification:

Tan JWY*, **Folz J***, Kopelman R, and Wang X. "In Vivo Photoacoustic Potassium Imaging of the Tumor Microenvironment." *Journal of Biomedical Optics Express*, 11 (2020), 2507-3522.

3.1 Introduction

Potassium is the most abundant cation in the body [9]. The evolution of live cells started by keeping Na^+ out of and K^+ inside the cell [148, 24]. Steep gradients exist in its distribution as intracellular K^+ concentrations are typically greater than 100mM [18, 9], while extracellular K^+ concentrations are approximately 5mM [9]. It has long been known that the tumor microenvironment (TME) can have suppressive effects on T cells [47]. However, this suppression was only recently attributed to disruptions in the K^+ concentration [29]. Notably, necrotic cell death in the nutrient-starved core of tumors leads to the release of vast quantities of intracellular K^+. The release of this K^+ induces local hyperkalemia in the TME with a reported 5-10 fold increase in K^+ concentration. In two seminal studies, Eil and colleagues determined that elevated

K^+ suppresses T cell effector function and prevents immune cells from maturing [29, 143].

In the previous analysis, the measurement of potassium was conducted via a specialized electrode - no *in vivo* measurements were made. Tumor interstitial fluid was collected by removing tumors from mice and centrifuging the tumor at such a speed so as to separate the tumor interstitial fluid from the solid tumor without lysing individual cells [149, 44, 43]. It was this fluid that was analyzed. Thus, all spatial and temporal information was lost in the analysis. As Eil and colleagues noted that T cell function was disrupted in a dose-dependent manner, it is of great interest to develop a method to measure potassium *in vivo*. The time-dependence, spatial-distribution, and extent of the tumor hyperkalemia remains uncharacterized.

An electrode is ill-suited for *in vivo* measurement due to its invasive nature and practical inability to gather spatial information. Few other methods exist to measure potassium beyond electrodes and their like. PBFI and the asante green series are the only commercially available potassium dyes. PBFI suffers from poor solubility and cellular uptake and both dyes are only excitable in the near ultraviolet spectrum. This dependence on high energy excitations is poorly suited to *in vivo* work as the light is quickly scattered. The alternative approach from using a dye is K^{39} MRI [49, 74]. K^{39} MRI has the advantage of measuring potassium in its natural environment and avoids completely the biodistribution problem associated with exogenous agents. However, MRI is an expensive technique, it is limited to patients without metallic implants, and continues to suffer from poor resolution (voxel size of approximately 1mL) [113].

Thus, to perform quantitative potassium measurements *in vivo* we adopted an pH-independent mechanism for sensing potassium. First developed by Eric Bakker

[155], this sensing mechanism is completely analogous to the KNP. However, instead using a pH dye as the optical reporter, a solvatochromic dye is used instead. Solvatochromic dyes' optical properties are highly sensitive to their environment. To make a sensor using them, a solvatochromic, positively-charged dye was conjugated to a long alkyl chain (18C). This renders the entire molecule hydrophobic, despite its positive charge. At low potassium concentration, these positive dyes remain in the hydrophobic interior of the nanoparticle due to the presence of anionic sites. As potassium concentration increases, an ionophore chelates potassium from solution, resulting in the addition of a positive charge to the interior of the sensor, which in turn pushes the positively charged dye head out of the particle's interior. The solvatochromic dye's absorption spectra changes due to the hydrophilic nature of the environment allowing for the measurement of potassium. Here, we use this sensor to measure the K^+ concentration in the TME and extend Photoacoustic Chemical Imaging (PACI) to incorporate K^+.

3.2 Methods

3.2.1 SD2 Synthesis and Characterization

1.5g 2-methylbenzothiazole and 3.8g 1-iodooctadecane were dissolved and refluxed in acetonitrile for 24 hours. The solution was removed from heat and allowed to solidify. The crude product was precipitated in diethyl ether, collected, and washed several times in diethyl ether. 265mg of this product, along with 122mg (dimethylamino) cinnamaldehyde, was then dissolved in acetic anhydride and refluxed for 20 minutes. The reaction solution was then poured into a warm solution of 10mM sodium iodide (in Millipore water). The dark purple precipitate was washed several times with water, dried, and collected. Measurements were made using positive ion electronspray mass spectrometry and performed by the University of Michigan's

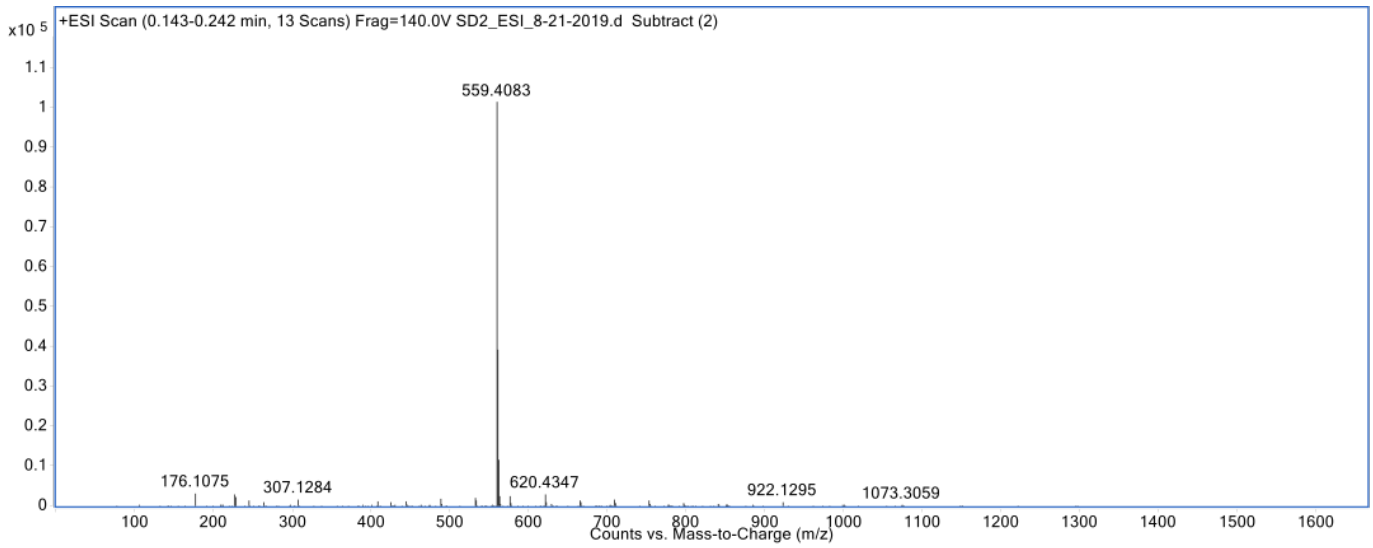

Figure 3.1: Mass spectrum of the synthesized and purified dye using the protocol described in the methods section. The reported mass of the dye was 559.5Da; we measured a mass of 559.4Da.

mass spectrometry core.

3.2.2 SDKNP Synthesis and Characterization

To generate a concentrated solution of nanoparticles, the following protocol was used. 0.2mg SD2 (synthesized in house, see above), 0.9mg sodium tetrakis [3,5-bis(trifluoromethyl) phenyl]borate, 1.2mg valinomycin, 5mg Pluronic F-127, and 8.75μL (8mg) dioctyl sebacate were dissolved in 3mL of methanol. The methanol cocktail was then injected into 30mL of Millipore water under vigorous stirring. The surface of the methanol-water mixture was blasted with nitrogen gas for 1 hour to remove the methanol. The nanoparticle solution was concentrated to the desired concentration using an Amicon Ultra-15 centrifuge filter (100kDa). Figure 3.2 shows the sensing mechanism *solvatochromic dye, potassium-sensing nanoparticle* (SDKNP) which is based on equilibrium exchange between an ionophore and a solvatochromic dye [155].

SDKNP size was evaluated using both Dynamic Light Scattering and Transmis-

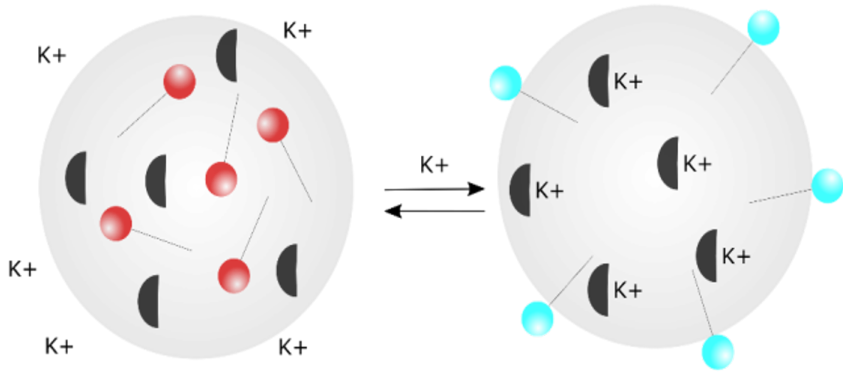

Figure 3.2: A schematic representation of the SDKNP sensing mechanism. The dark half circles represent potassium ionophore while the ball and stick models represent the solvatochromic dyes. At low potassium concentration, all dyes remain in the hydrophobic interior of the nanoparticle. As potassium concentration increases, it is chelated from solution by the ionophore. This chelation forces the dye head from the interior of the particle to its surface, where its sensitivity to the environment results in a change in absorption.

sion Electron Microscopy (Figure 3.3). DLS measurements show the particles of an average diameter of 90nm with polydispersity index of 0.107. Zeta potential measurements indicated that the SDKNP is highly stable, with a zeta potential of -69.0mV. Dynamic Light Scattering and Zeta-Potential measurements were performed at a nanosensor concentration of 1mg/mL using a Beckman Coulter analyzer.

3.2.3 SDKNP Toxicity

HeLa cells (ATCC authenticated) were cultured in Dulbecco's Modified Eagle Media with 10% fetal bovine serum and 1% penicillin/streptomycin. 100,000 cells were plated on a 24 well plate and allowed to grow over night in 1mL of growth media. SDKNPs were incubated for various times at a concentration of 1mg/mL. Following incubation, 500μL of incubation media was replaced with 500μL of MTT solution (5mg/mL in PBS) and incubated for 4 hours. Once finished, all media was removed from the wells and replaced with 1mL of DMSO. This solution was then incubated for 1 hour at which point the solution was removed and its absorption

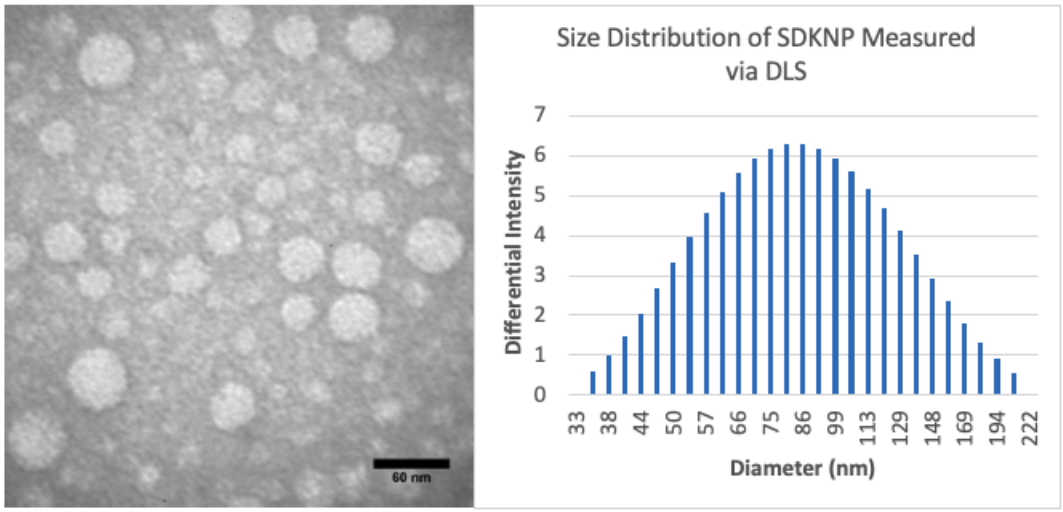

Figure 3.3: Left) TEM image of the SDKNP. Right) Dynamic Light Scattering distribution for the SDKNP. The SDKNP has an average diameter of 90nm and a polydispersity index of 0.107.

spectrum measured in a UV-VIS spectrophotometer. Absorption peaks at 590nm were compared, and all samples were repeated four times. Figure 3.4 shows that the SDKNP is toxic, especially beyond 6 hours of exposure.

3.2.4 Inductively Coupled Plasma Mass Spectroscopy

Tumor interstitial fluid was diluted with Millipore water by a factor of 5000 prior to measurement with a Perkin-Elmer Nexion 2000 ICP-MS (Perkin-Elmer, Waltham, MA, USA). The machine was calibrated using standards prepared at 50, 100, 250, 500, and 750PPB K^+ using potassium chloride as a source for K^+ ions.

3.2.5 PA and UV-VIS Calibrations

For the UV-VIS calibration, K^+ calibration samples of 0, 1, 5, 10, 20, 30, 50, 70, 100, and 150mM K^+ with 1mg/mL of SDKNP were prepared. Samples were prepared in pH 7.4 MOPS-buffered saline solution containing physiologically relevant concentrations of interfering cations: sodium (150mM), magnesium (1mM), and calcium (2.6mM). The absorption spectrum for each sample was obtained for a range of

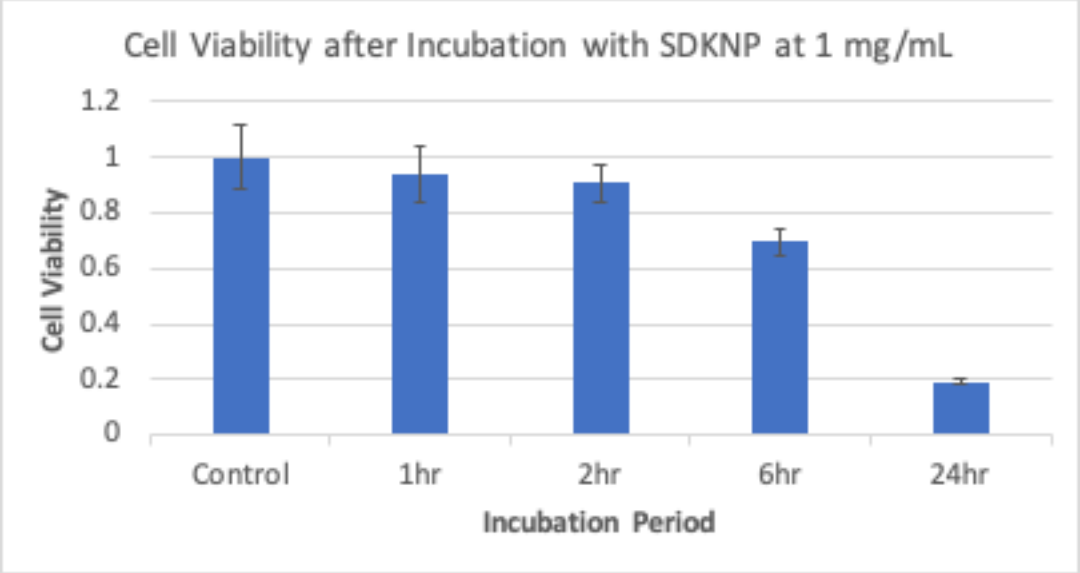

Figure 3.4: An MTT assay shows the SDKNP is toxic, and the toxicity increases with exposure time, though approximately 90% of cells are viable within 2 hours of exposure.

400-800nm using a Shimadzu 1600 UV-VIS Spectrophotometer (Shimadzu, Kyoto, Kyoto, Japan). For the PA calibration, K^+ calibration samples of 0, 1, 5, 10, 20, 30, 40, 50, 70, 100, and 150 mM K^+ with 10mg/mL of SDKNP were prepared. 75μL of each sample was added into a transparent PVC tubing. The tube samples were submerged in water for acoustic coupling. The tube samples were then imaged using a PACI system consisting of a tunable pulsed laser (Continuum, Santa Clara, CA, USA) and a 128-element ultrasound probe with frequency range of 7 to 15 MHz (CL15-7, Philips, Andover, MA, USA)). The tunable pulsed laser pumped by the third harmonic of an Nd:YAG laser (Continuum, Santa Clara, CA, USA), has a pulse duration of 5ns, a firing frequency of 10 Hz, and is capable of achieving wavelength tuning in the range of 410-680nm and 710-2500nm. The ultrasound probe was then connected to a commercially available research ultrasound platform (Vantage 256, Verasonics, Kirkland, WA, USA) for data acquisition. A general PA imaging setup is shown in Chapter 1. The PA signal was obtained for 6 wavelengths of 545,

560, 576, 584, 605, and 625 nm, chosen based on the absorption spectra obtained. Each PA signal was averaged 20 times, with a total of 4 replicates performed for each sample. A simple light fluence correction was performed where the PA signal was normalized to the average energy measured for each wavelength using a power meter (Newport, Irvine, CA, USA).

3.2.6 PA Multi-wavelength Unmixing

An identical setup to the PA calibration experiment was performed. K^+ samples of 2, 5, 20, 40, 50, and 150mM were prepared in the presence of 1% blood v/v and 10mg/mL of SDKNP as well as a blank sample which only contained saline solution. PA imaging was conducted for 6 wavelengths of 545, 560, 576, 584, 605, and 625nm. The wavelengths were chosen based on the isosbestic points and maximal difference in the extinction coefficients of SDKNP and hemoglobin. Multi-wavelength unmixing was performed according to the following steps. Firstly, at each wavelength, the PA signal can be modeled as shown below:

$$PA_\lambda = k(\varepsilon^\lambda_{Hb}[Hb] + \varepsilon^\lambda_{HbO_2}[HbO_2] + \varepsilon^\lambda_{NP}[NP]) \tag{3.1}$$

where λ is the wavelength in nm, [SDKNP] is the SDKNP concentration, [HbO_2] is the oxyhemoglobin concentration, [Hb] is the deoxyhemoglobin concentration, ε is the extinction coefficient, and k is a constant associated with multiple parameters such as light fluence, the Gruneisen parameter of the sample, and the sensitivity of the imaging system. It should be noted that ε_{SDKNP} is dependent on both λ and the K^+ concentration.

The extinction coefficients of Hb and HbO_2 for each λ are known values, while the extinction coefficient of SDKNP can be measured at each λ and for a range of K^+

values. Here, we measured the value of ε_{SDKNP} for K^+ values of 0, 1, 5, 10, 20, 30, 40, 50, 60, 70, 80, 90, 100, 125, 150, and 200mM using a UV-VIS spectrophotometer. This left only 4 unknowns in the above equation, specifically [SDKNP], [HbO_2], [Hb], and [K^+]. Using simple linear algebra, the 4 unknowns can be solved by making at least 4 separate measurements at different wavelengths. Here, we used 6 wavelengths to solve the linear equations for increased accuracy, as it is widely known that additional measurements can help to improve the accuracy of the unmixed results. [28, 95, 39]. A notable limitation to this technique is that the estimation of the [K^+] is based on measurements of the extinction coefficient of the SDKNP at discrete K^+ values, meaning that the values of the measured K^+ are always limited to those discrete K^+ values. An alternative to this is to model the ε_{SDKNP} response to K^+ by using an equation-based approach. This approach, while allowing for continuous K^+ estimates, has its own drawbacks in that no simple equation model can perfectly capture the ε_{SDKNP} response to K^+, meaning that approximations will have to be made, reducing the accuracy of the measurements.

3.2.7 *In vivo* PA Imaging of K^+

Animal care was provided by the Unit for Laboratory Animal Medicine (ULAM), and all procedures on live animals were performed in accordance with institutional guidelines and approved by the Institutional Animal Care and Use Committee (IACUC) at the University of Michigan. A total of 6 mice were used in the i*in vivo* imaging experiment. To generate the subcutaneous tumors, approximately 1x106 9L glioma cells (ATCC, Manassas, VA, USA) in 0.1mL of RPMI 1640 (Gibco, Waltham, MA, USA) was injected into the thigh muscle of 5-week old nude mice (Envigo, Huntingdon, Cambridgeshire, UK). The tumors were allowed to grow till a size of approximately 1cm in diameter. 0.05mL of 10mg/mL SDKNP was then locally injected

into the tumor, followed by PA imaging immediately after the injection. This was repeated with the thigh muscle on the opposite flank, where 0.05mL of 10mg/mL SDKNP was locally injected in the thigh muscle, followed by PA imaging immediately after the injection. All PA imaging was conducted for the same 6 wavelengths of 545, 560, 576, 584, 605, and 625nm, with a total of 80 averages per image. A simple light fluence correction was performed where the PA signal was normalized to the average energy measured for each wavelength using the power meter. Multi-wavelength unmixing was conducted according to the same protocol as previously mentioned with the exception that only K^+ values between 0-125mM were analyzed. This range was chosen to reflect the expected biological range of the extracellular tumor K^+. After the imaging, the mice were euthanized, and the tumor harvested. An adaptation of the protocol performed by Eil et al. was conducted to collect the extracellular fluid from the tumor[29]. Briefly, the tumor was first flushed with saline to remove surface blood and blotted gently with Kimwipe (Kimberly-Clark, Irving, TX, USA) to dry. The tumor then was placed in a SpinX centrifuge tube filter (Corning, New York, NY, USA) and centrifuged at increasing speeds of 1000, 2000, 4000, and 8000RPM for 10 minutes each [43]. Approximately 4-10μL of extracellular fluid was collected per tumor. The extracellular fluid was then sent for ICP-MS.

3.3 Results

We adopted a potassium sensor for the photoacoustic quantification of potassium. To test the capabilities of the SDKNP for PACI of K^+, we first compared the response of the SDKNP to K^+ using both PACI and UV-VIS spectrophotometry. Figure 3.5a shows the absorption spectra obtained for SDKNP at various K^+ levels. The largest absorption change occurred at 605nm for the changing K^+ concentrations, with a

small opposite trend at around 545nm. The isosbestic point of the SDKNP is at approximately 560nm. Making use of these wavelength ranges, the PA and UV-VIS calibration ratios were plotted in Figures 3.5b-f. These calibration ratios show the changes in the PA and the UV-VIS signals with respect to the isosbestic point for increasing concentrations of K^+. As the PA signal of a molecule is directly proportional to its absorption, the PA calibration is expected to match that of the UV-VIS calibration. To show the good agreement between the PA and UV-VIS measurements, the ratios are co-plotted in Figures 3.5b-f to show the similarity between the ratios measured by both modalities. These ratios generally showed a signal decrease with increasing K^+ concentration, with exception of the 545nm/560nm ratio. The SDKNP is most sensitive between 0-50mM K^+, an ideal range for the expected *in vivo* tumor K^+ concentration. Based on these results, we used the UV-VIS spectrophotometer measurements for later calibrations, as they generally provided measurements with very low noise levels.

Next, we analyzed the capability of separating the SDKNP signal from the expected *in vivo* endogenous chromophores of deoxyhemoglobin (Hb) and oxyhemoglobin (HbO_2). While other chromophores such as melanin and water are also present in biological tissue, Hb and HbO_2 are expected to be the major PA signal contributors within the 545-625nm wavelength range in the tumor. Using a similar setup as the calibration experiment, multi-wavelength unmixing was performed for various K^+ samples in the presence of 1% blood v/v. This volume of blood was used as it is close to the estimated blood volume fraction in a tumor tissue (for breast cancer) [129]. Using a 6-wavelength unmixing technique, the concentrations of K^+, SDKNP, Hb, and HbO_2 were identified with the results shown in Figure 3.6. The Hb and HbO_2 concentrations were then combined, as the oxygenation of the sample was not

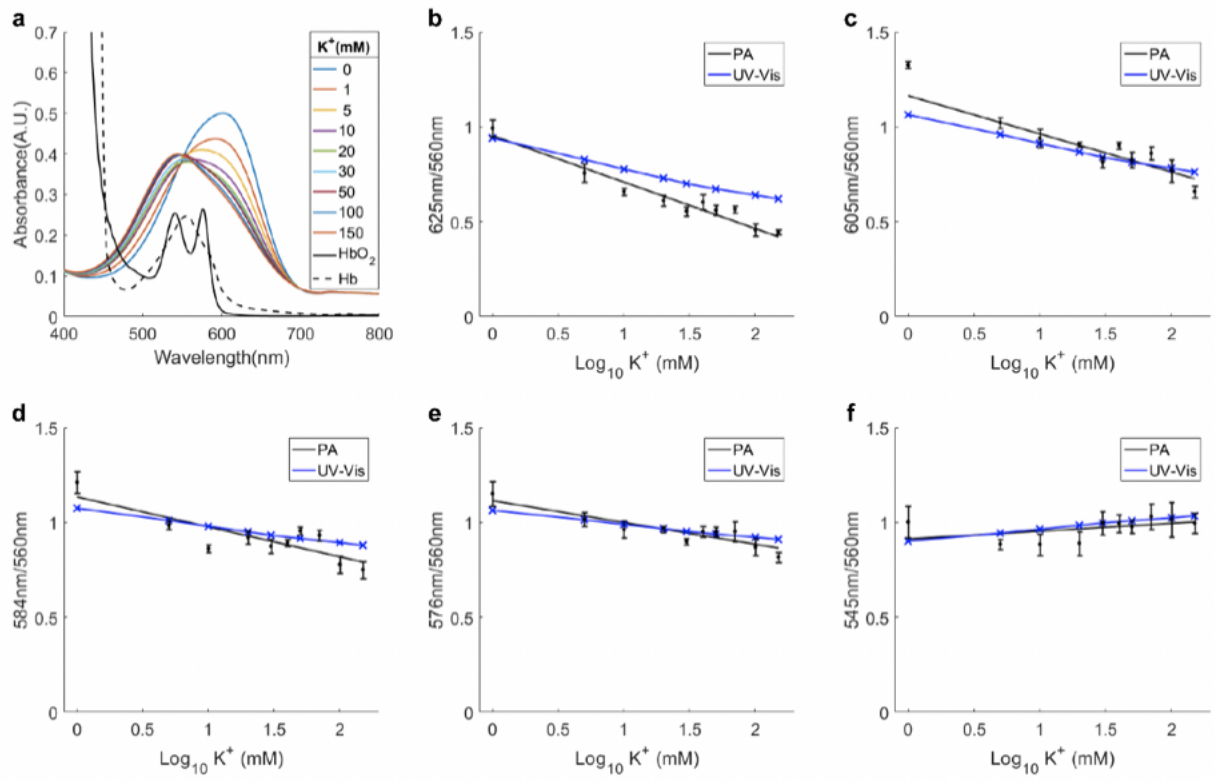

Figure 3.5: Absorption spectra and PA K^+ calibrations compared to UV-VIS K^+ calibrations. (a) Absorption spectra of SDKNP for various K^+ concentrations, oxyhemoglobin (HbO2), and deoxyhemoglobin (Hb). PA and UV-VIS ratio measurements for (b) 625nm/560nm, (c) 605nm/560nm, (d) 584nm/560nm, (e) 576nm/560nm, and (f) 545nm/560nm. There is excellent agreement between the PA and UV-VIS calibrations.

controlled and the total hemoglobin (THb) concentration was expected to serve as a more precise measurement. Within the SDKNP's sensitivity range of 0-50mM, the unmixed measurements of K^+ concentration showed good accuracy levels (+/-5mM), with exception of the 20mM sample. Outside this range, the measurement accuracy drops rapidly, although qualitative increases can be observed, as is shown by the significantly lower PACI estimate of 76mM for the 150mM K^+ sample. There is also some noticeable bleed through of the SDKNP and blood signals at higher K^+ concentrations. This is most likely due to the absorption spectra of the SDKNP being more similar to blood at higher K^+ concentrations, especially that of deoxyhemoglobin (Figure 3.5a). It should be noted that this does not affect the K^+ measurement significantly, as most of the error is localized in the [SDKNP] and [THb] measurements. Finally, the blank sample showed almost no detectable signal throughout, as expected.

After verifying the ability to measure the K^+ signal *in vitro* in the presence of blood, we then tested the ability to perform *in vivo* measurement of K^+ in a subcutaneous tumor mouse model. We locally injected 0.05mL of 10mg/mL SDKNP into the tumor and the thigh muscle of the mice before conducting PACI at the 6 wavelengths. Figure 3.7a shows an example of the map of oxygen saturation, SDKNP concentration, and K^+ concentration in the tumor and the muscle as measured by PA multi-wavelength unmixing for an individual mouse. Figure 3.7b shows the average hemoglobin oxygen saturation across all mice (n=6). While there is a slight decrease in the average tumor hemoglobin oxygen saturation compared to the muscle (47.5% compared to 52.3%), it was not statistically significant in this study. Figure 3.7c shows the average SDKNP concentration across all mice, where there was no significant difference detected between the tumor and the muscle). As equal con-

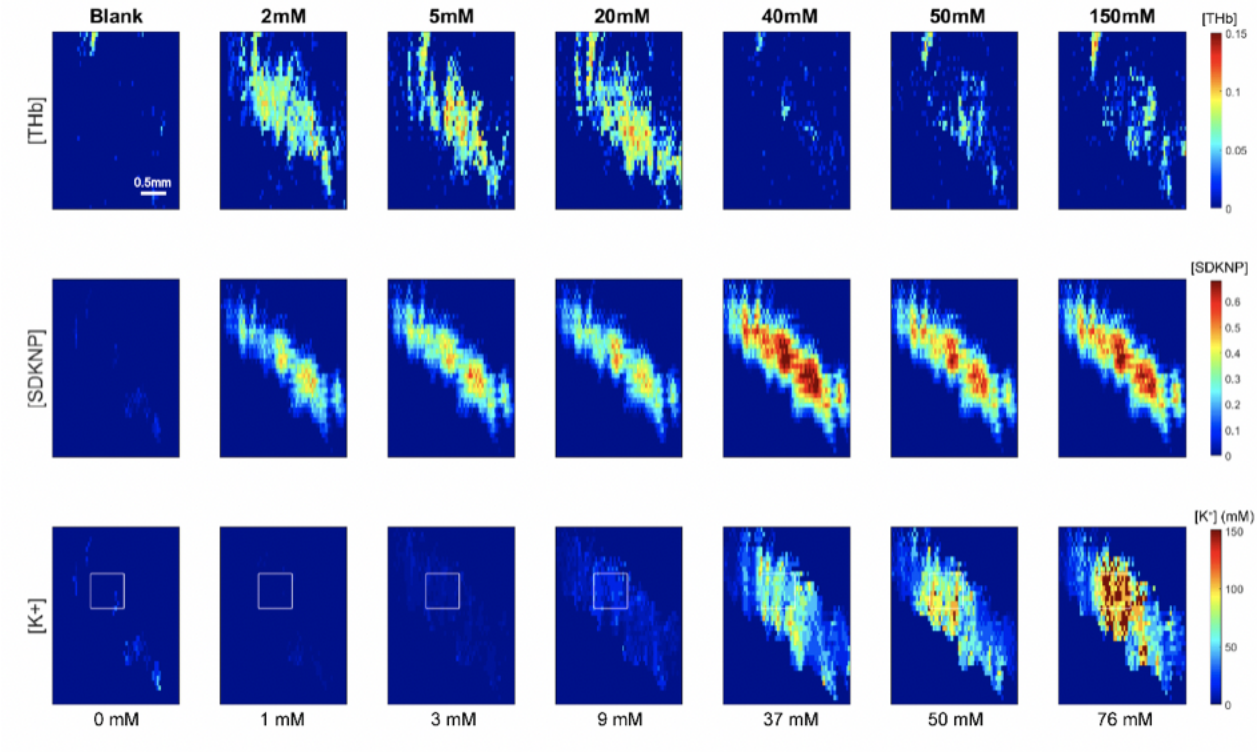

Figure 3.6: PA multi-wavelength unmixing for SDKNP samples in a tube for determining total hemoglobin concentration ([THb]), SDKNP concentration ([SDKNP]), and K^+ concentration ([K^+]). All samples contain SDKNP and 1% blood v/v at the specified K^+ concentrations, with exception of "Blank", which only contains saline solution. Sample values of K^+ are provided at the top of the figure, while the measured values obtained via deconvolution are given at the bottom of the figure. Measured values pertain to the average K^+ in the region of interest outlined by the white box.

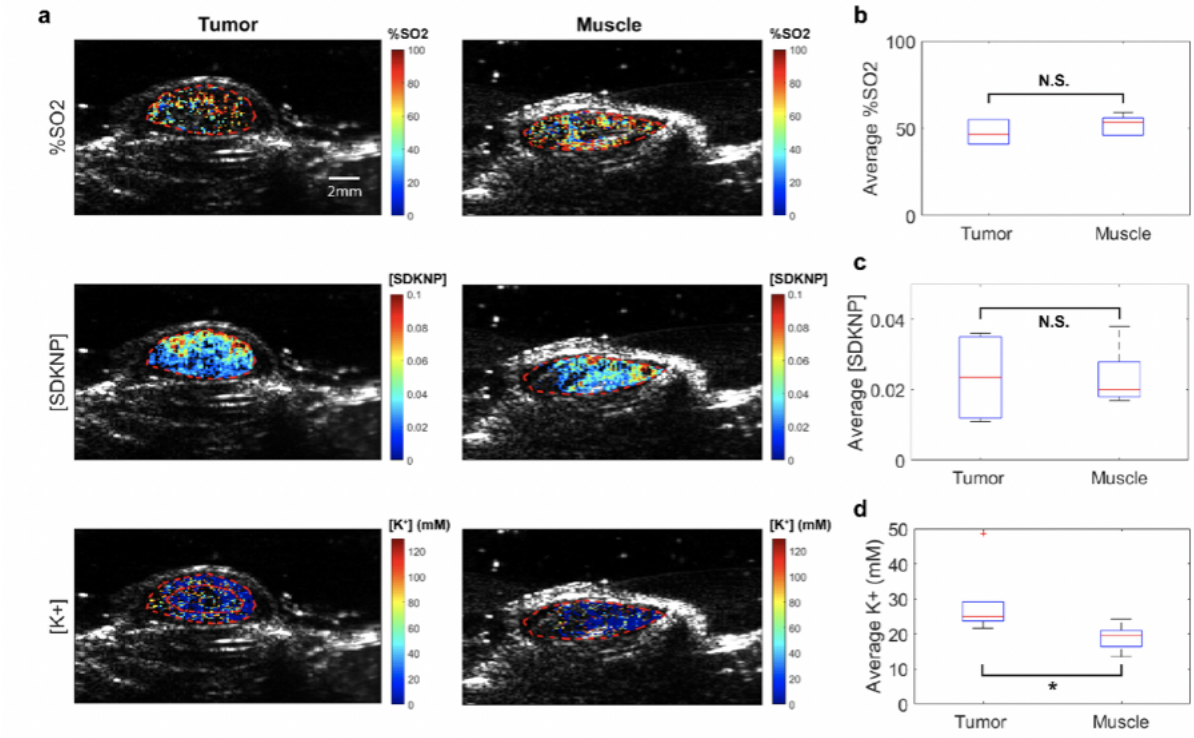

Figure 3.7: *In vivo* PA imaging with overlaid ultrasound images of subcutaneous tumors and thigh muscles (control) in nude mice. (a) Multi-wavelength unmixing performed to identify the hemoglobin oxygenation saturation (%SO2), SDKNP concentration ([SDKNP]), and K^+ concentration ($[K^+]$). The average value across all mice (n=6) in the tumor and the muscle for (b) %SO2, (c) [SDKNP], and (d) $[K^+]$, as determined by multi-wavelength unmixing. 'N.S.' indicates no significance, '*' indicates p less than 0.05.

centrations of SDKNP were injected into the tumor and the muscle, this result was expected. Figure 3.7d shows the average K^+ concentration between the tumor and the muscle, where the tumor K^+ was significantly higher than the muscle K^+. We observe an average K^+ concentration of 29mM (range of 22-49mM) in the TME, as expected from the predicted 5-10 fold increase [29, 143]. In the muscle samples, we see an average concentration of 19mM (range of 14-24mM), which is higher than naively expected.

To validate the accuracy of the K^+ measurements *in vivo*, we then measured the average K^+ within the tumor via a method involving centrifugation to extract the

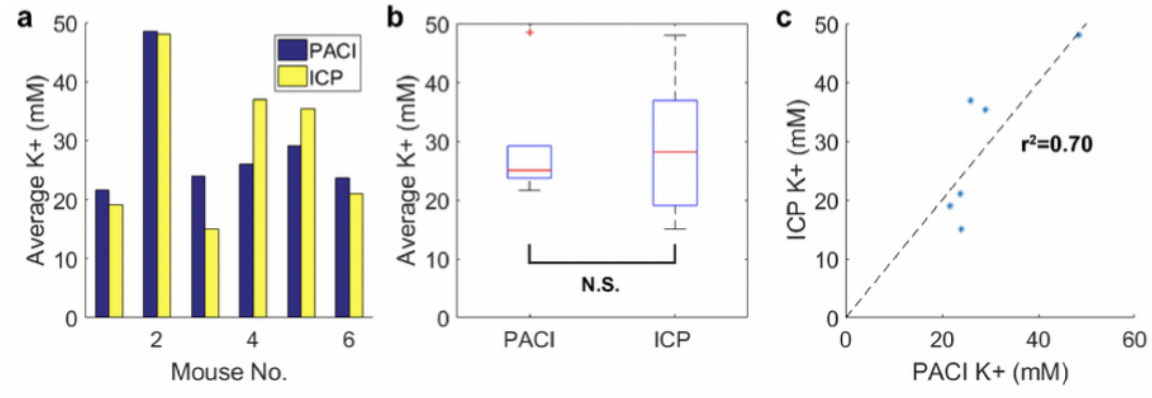

Figure 3.8: Average K^+ measurement in the tumor from PA imaging vs ICP. Average K^+ in the tumor for (a) individual mouse measurements, and (b) across all mouse samples (n=6). 'N.S.' indicates no significance. (c) Correlation analysis between the ICP and the PACI measurements.

interstitial fluid of the tumor, followed by inductively coupled plasma mass spectroscopy (ICP-MS) to measure the K^+ concentration of the extracted fluid. The centrifugation method was used by Eil et al. to measure the K^+ concentration of the tumor [29]. The results of the ICP measurements are compared to the PACI measurements in Figure 3.8. Figure 3.8a shows the average K^+ concentration measured by PACI vs ICP for each of the individual mouse tumors. Figure 3.8b shows a box plot of the distribution of average K^+ measurements for PA imaging and ICP. Here, the mean value of K^+ measured using PACI was 29mM (range of 22-49mM), identical to the ICP value of 29mM (range of 15-48mM). Figure 3.8c shows the correlation between the average K^+ measurements made by PACI as compared to the ICP measurements. Generally, there was good agreement between the two K^+ measurements, with a correlation value of 0.70.

To further analyze the capability of our PACI technology for detecting spatial information within the tumor, we analyzed the K^+ distribution within the tumor core and the periphery. As it has been reported that the necrotic core was the cause

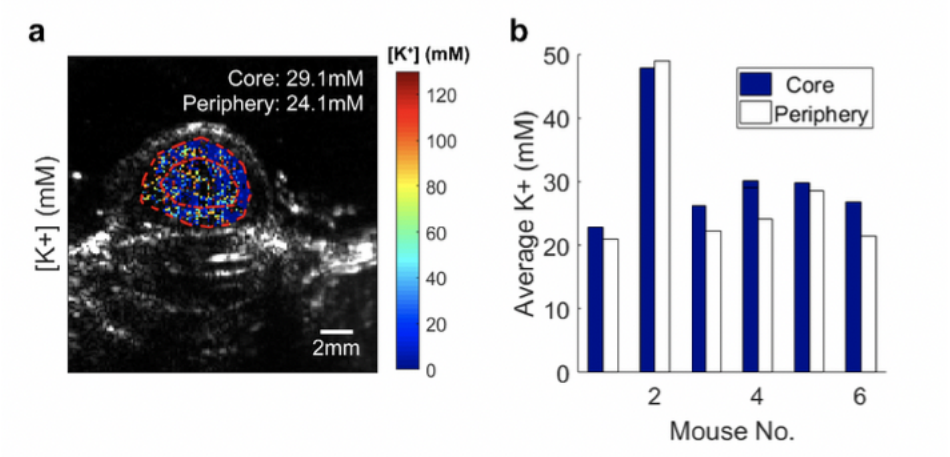

Figure 3.9: Further analysis of the measured K^+ within the tumor core vs the tumor periphery. (a) An overlaid PA and ultrasound image showing the regions of interest of the core and the periphery, outlined in red. (b) Measured K^+ concentrations for each mouse for the tumor core and the tumor periphery.

of the elevated K^+ in the tumor, we wanted to identify if there was a difference in the K^+ concentration within the tumor core (where the necrotic cores are expected), as compared to the peripheral regions of the tumor. Based on this, we would expect to see a higher K^+ concentration in the tumor core as opposed to the periphery. The results of our analysis are shown in Figure 3.9, where an example of the determined regions of interest are shown in Figure 3.9a. The cores were demarcated by taking a region of approximately 40% of the entire demarcated tumor, centered around the estimated geometric center of the tumor. Here, we noted that there was an increase in the measured K^+ concentration in the tumor core for almost all the tumors (Figure 3.9b), although this increase was small (3mM or 10% higher). These observations suggest that elevated K^+ within tumors may not be uniform, and that this spatial difference can potentially be detected via PACI.

3.4 Discussion

In this study, we demonstrate the ability of PACI to measure the K^+ concentration in a tumor *in vivo*, and show the elevated K^+ concentration in the tumor compared to the muscle tissue. These results were verified using ICP-MS with good correlation between the two independent measurement techniques (r^2=0.70). While Eil et al. have demonstrated that TME hyperkalemia induces elevated intracellular K^+, it remains unknown at what K^+ threshold this suppressive effect manifests itself. The ability to measure K^+ concentrations *in vivo* could provide an essential tool to the field of immunology, with studies no longer having to rely on *in vitro* measurements of K^+ at single time points with no spatial resolution. Additionally, an example of the spatial distribution of the TME hyperkalemia, as measured by our PACI technique, have been provided here. While the observed tumor K^+ heterogeneity was small, this may not be the case at a different time point of the tumor's development, especially at long times and large tumors. PACI of K^+ is ideally suited for characterizing these physiological phenomena, allowing for quantitative and spatial measurements of K^+ in an *in vivo* mouse tumor, and potentially in a patient's tumor.

There are still improvements that can be made with the K^+ measurement. Regarding the discrepancies seen in Figure 3.6, besides instrument calibration errors (UV-VIS spectrophotometer, ICP-MS), the PACI errors are mainly attributed to inaccuracies in the multi-wavelength unmixing technique, due to the wavelength-dependent light fluence attenuation in the sample, namely the "rainbow effect", and the wavelength-dependent laser energy output. While the latter is mostly corrected for by monitoring the laser energy through the partial reflector in the setup, the former is significantly more challenging to correct. A significant amount of research

has been dedicated to this area, where methods to model the light fluence distribution in a tissue sample are being studied [65, 3, 62]. Without this wavelength-dependent light fluence correction, quantitative PA imaging is usually limited to surface/subcutaneous tumors. In a previous study, we have shown good accuracy within 6mm depth from the tumor surface [52]. Besides light fluence modeling, increasing the number of wavelengths used in the imaging and multi-wavelength unmixing can also improve the accuracy of the measurements [28, 95, 39]. The latter method, however, has its own drawbacks in that the imaging time will be significantly increased, depending on the number of wavelengths desired.

Additionally, there are some concerns regarding the toxicity of the current formulation of the SDKNP. While not having significant toxicity within 2 hours, prolonged exposure does cause significant cell death in an MTT study. This toxicity is largely attributable to the use of valinomycin as the K^+ ionophore. However, there are adjustments that can be made to the nanoparticle matrix to allow for substitution with a less toxic ionophore, such as BME-44. Notably, the Pluronic polymer is highly biocompatible and in wide medical use [6]. That being said, the strength of using these ionophore-based optical sensors is the relative ease at which sensors for other materials can be developed. For example, substituting valinomycin for a sodium ionophore allows for the development of a PA sodium sensor with relative ease. Additional substitution of ionophores and plasticizers would allow for sensing multivalent cations, such as magnesium, calcium, or transition metal ions, though non-trivial adjustments would be required, especially as the physiological concentrations of these species are much lower than that of K^+.

CHAPTER IV

Morphodynamic Cell Phenotype Classification with application to Cancer

This chapter has been adapted from the following publication to add additional data and emphasize personal contributions:

Elbez R*, **Folz J***, McLean A, Roca H, Labuz JM, Pienta KJ, Takayama S, and Kopelman R. "Morphodynamic Cell Phenotype Classification with application to Cancer" *in submission* '*' indicates co-first author

4.1 Introduction

Cancer lethality is overwhelmingly due to metastasis, the process by which cells from the original cancerous tumor leave their environment and disseminate to colonize new tissues [106]. During this metastatic process, motile cells escape the original tumor by intravasation. Separated single cells or multi-cellular clusters migrate through the extra-cellular matrix (ECM) surrounding the tumor, passing through the endothelium into the bloodstream. Upon entering the bloodstream, cells and clusters are buffeted by hemodynamic forces on the range [88, 145] of 4-30 dyns/cm^2. Additionally, these cells must contend with immunological insults and collisions with red blood cells. Having survived under these conditions, cancer cells must latch onto epithelial cells and extravasate into "foreign" tissue, so as to seed a secondary tumor.

To survive this gauntlet of challenges, metastatic cells must express entirely different phenotypes than their stationary counterparts. Specifically, the epithelial to mesenchymal transition (EMT) permits the relatively stationary, epithelial cells of solid tumors to obtain the mobility required so as to intravasate and exit the primary tumor. It has been observed that the post-EMT amoeboid-like cells can significantly increase the metastatic potential of the tumor [53], and morphological changes can be used to identify cells having undergone the EMT [163]. Morphology has been further used to predict the metastatic potential of osteosarcoma cells [25, 133], and has been used to differentiate chemoresistant and chemosensitive cell lines [5, 4]. Work in linking cell morphology to phenotype has come from the group of Chris Bakal, which has developed a method for probing the relationship between individual genes and morphology [17]. They have shown a quantitative link between cell morphology and Rho GTPase signaling pathways [99, 104], and also claimed that transitions between cell morphologies are switch-like rather than gradual [160].

To date, most studies of cell morphology have focused on plated, adherent cell lines. Notably, even though clear morphological distinctions can be discerned among cells when plated, the mere two-dimensional plating process might change their phenotypes and thus alter the quality of the diagnostics [19, 1, 11, 125, 33]. Furthermore, adherent cells are restricted from freely exhibiting potential morphological changes or morphodynamic behavior, i.e., the morphological changes in individual cells and populations over time. Here cell morphodynamics describes a cell's "plasticity" or "shape shifting" capability. Thus, in this study, we combine cell magneto-rotation with machine learning so as to examine cellular morphodynamics. Machine learning has lent itself to many medical applications [161]; our approach allows researchers to probe cell motility and morphological expression.

Operationally, GFP expressing cancer cells are activated by endosomic uptake of magnetic nanoparticles, are loaded into a microfluidic device that contains an array of microwells, and remain non-adherent while rotating in an oscillating magnetic field. This allows 3-dimensional cell deformations, akin to their *in vivo* behavior. Most microwells contain a single cell, and in each microwell, the cell is free to take any shape in its morphological space. After taking fluorescent images of these cells, we combine object recognition and machine learning algorithms so as to differentiate, cluster, and identify each of the cells by its morphological profile. We found that cells having undergone the EMT could be distinguished from control cells, which demonstrates a morphodynamic equivalent of a change in protein expression. Furthermore, highly migratory cells were also found to be morphodynamically distinct from a control population. This new machine learning (ML) based method appears to have the potential to reliably map and classify the morphological distribution of a cell population, and thus to provide information on a tumor cell population's degree of morphological plasticity, which may be related to its lethality. We have used this method here to demonstrate the strong relationship between a cell's morphological and biological behaviors.

4.2 Methods

4.2.1 Preparation of Magnetic Nanoparticles (MNPs)

Amine-coated magnetic nanoparticles (Ocean Nanotech) with a diameter of 30nm, are prepared in a 1mL stock solution of 200μg/mL in cell culture media. We then add 15μL of Poly-L-Lysine at 0.1%w/v (Sigma-Aldrich), and the solution is left for an hour on a rotator at room temperature. The solution is then filtered using a 0.2μm syringe filter.

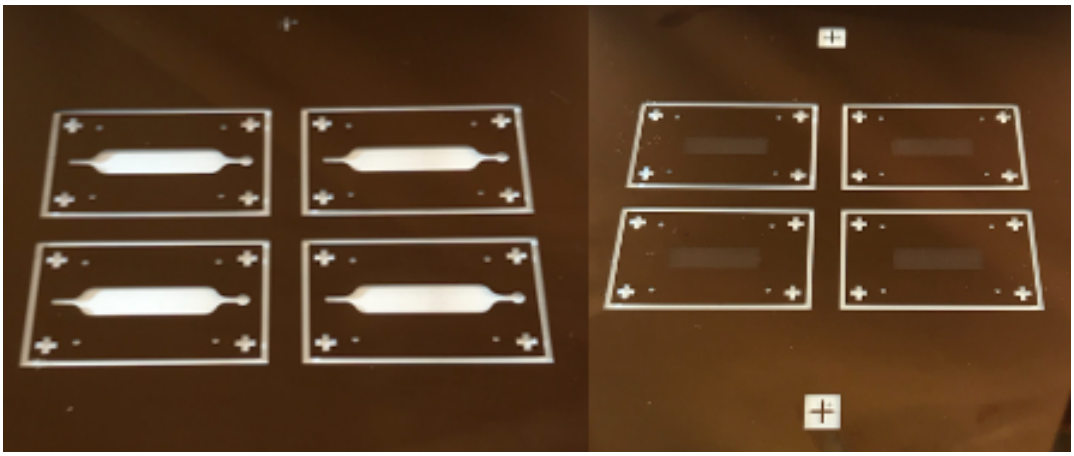

Figure 4.1: Photographs of the microfluidic masks. These masks are used during contact lithography to cure SU-8 in the illuminated pattern. The masks on the left is the first layer, which consists of the canal. The pattern on the right contains the array of triangular microwells that are used to capture the cells.

4.2.2 Cell Culture and Magnetization

Cells were purchased from and verified by ATCC. All cell lines were stably expressing GFP. MCF-7 and MDA-MB-231 cells were cultured in DMEM supplemented with 10% FBS and 1% Penicillin- Streptomycin- Glutamine in a 37°C with 5% CO_2 and 100% humidity. Cells' confluency before addition of the MNPs is around 20-30%. Cells are incubated for 24 hours with cell culture medium to which is added (see below) 20μg/mL of amine-coated magnetic nanoparticles. These particles are uptaken via endocytosis.

4.2.3 Microfluidic Mask Making

Microfluidic devices were prepared as described by Park [60]. Masks were produced at the University of Michigan's Lurie Nanofabrication Facility using the Heidelberg μPG 501 Masker Maker. The masks for the two layer device are shown in Figure 4.1.

4.2.4 Microfluidic Mold Manufacture

Using the masks, a mold for the microfluidic devices is produced. Briefly, a was vacuumed sealed to a Solitec Spinner. Approximately 1mL of SU-8 2000 was poured onto the wafer, after which it was spun at 1500RPM to induce a 200μm thick coating. The wafer was removed from the spinner, and placed in dark, flat space for 24 hours so as to remove dissolved gases from the SU-8. Prior to lithography, the wafer was prebaked at 60°C for 10 minutes. Contact lithography was performed using the Karl Suss MA 45s. The device was exposed as per the SU-8 manufacturer's specifications. Following lithography, the wafer was washed with Su-8 developer to produce features. Undeveloped SU-8 was removed with acetone and isopropyl alcohol. The device was given 24hours to dry before it was cleaned and the second layer applied in the same manner as the first. The second layer uses SU-8 1500 spun at 3000RPM, and requires no rest time due to the viscosity of SU-8 1500 and the relative thinness of the second layer. Once the second layer has been developed, the wafer is thoroughly cleaned using acetone and isopropryl alcohol. The mold is placed in a vacuum chamber with PDMS-release dissolved in toluene. The vacuum is applied for approximately 5minutes to induce a low vapor pressure in the chamber, and then is sealed. The chamber is left for 24 hours to allow proper deposition of PDMS release. Following the 24 hours, the mold is ready for use.

4.2.5 Microfluidic Device Manufacture

To make microfluidic devices, one each of a prepared mold and a blank wafer are placed in miniature 4 inch pie tins. The blank wafer is required, as it will form the top layer of the microfluidic device. For each mold, 40g of polydimethylsiloxane (PDMS) and 4g of curing agent. The two are mixed thoroughly via mechanical stirring for at

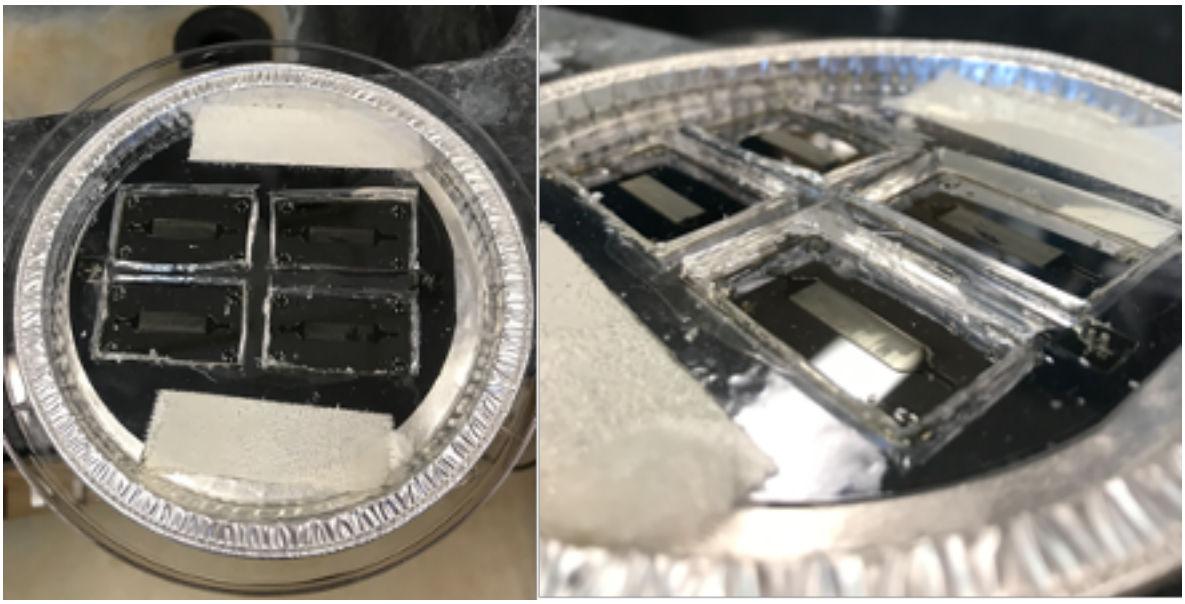

Figure 4.2: Pictures of a microfluidic mold with improper PDMS-release deposition. The images show the cured PDMS sitting on the mold. The devices (rectangles) have been cut out of the PDMS layer. On a mold with quality PDMS-release deposition, all of the PDMS can be peeled off as a single piece.

least 3 minutes. Then the 44g mixture is poured onto of the device in the pie tin. It is then moved to a vacuum chamber where the mixture is fully degassed over several rounds of depressurization. Once the gases have been removed, the PDMS is baked at 100°C for 24 hours to cure the PDMS. After baking, the individual devices are cut out of the mold. The bottom and top layer are attached by activating the PDMS in the Glen 100P Plasma Cleaner. Once the top and bottom of the device are attached, the PDMS is further activated and rendered hydrophillic. Phosphate-buffered saline is injected into the inlet port, and the devices are stored until use.

4.2.6 Microfluidic Trapping System and Cell Loading

One hour before being exposed to fluorescent light, cells are washed with Hank's Balanced Salt Solution (HBSS) three times to remove traces of phenol red contained in the cell culture media, and then incubated for an hour in a colorless cell culture

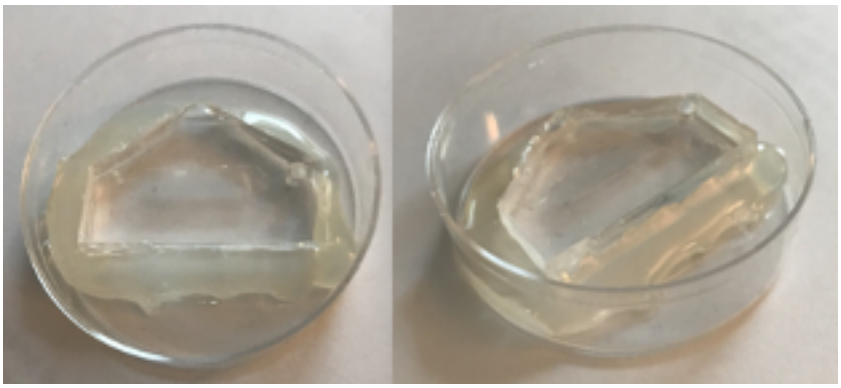

Figure 4.3: Photographs of the prepared microfluidic device. The devices are hot-glued into 60mm Petri-dishes, which are then filled with 37°C water to mimic *in vivo* conditions.

media that has been supplemented with the radical oxygen scavenger, Trolox (6-hydroxy-2,5,7,8-tetramethylchroman-2-carboxylic acid, Sigma-Aldrich), at 0.25nM. After an hour, cells are washed with HBSS, and gently detached using a cell scraper. Cell density is then adjusted by the help of a magnetic separator.

Cells are then gently pipetted into the microfluidic device (Figure 4.3). Each well has a triangular shape, with a side size of 40μm and a depth of 35μm. The chip has two ports: An inlet port and an outlet port. Cells are loaded with a 100μL pipetter into the inlet, and gently introduced into the channel by applying negative pressure at the outlet. Once positioned, the device is put on top of a rare earth magnet to pull the cells down into the wells. We repeat these steps several times, until a sufficient loading ratio is achieved (above 60% of the traps occupied by single cells). These loading steps take around 3 minutes, and no more than 5 minutes. Finally, cells are washed with fresh media by gently pipetting fresh media into the device (fresh media is placed at the inlet port and pipetted from the outlet port). At the end of the imaging series, propidium iodide is pipetted into the inlet port and the cells are imaged so that dead cells can be removed from the analysis.

4.2.7 Cell Imaging and Rotation

Cells are imaged on an Olympus IX71 microscope, equipped with an arc-mercury lamp (U-RX-T) and a high definition monochromatic digital camera (Q-Imaging Retiga 6000, 10 Megapixels). To image simultaneously multiple positions of the device, the microscope stage is replaced with a motorized stage (ASI MS-4400 XYZ Automated Stage). Images are captured with the software package Micro-Manager (extension of ImageJ), while the stage is programmed and controlled via a custom made script in Micro-Manager [97]. To protect cells from light exposure, a custom made shutter opens for 700ms at every position each minute. Only single cells are kept to be measured. Temperature and humidity are controlled using a homemade, on-stage system that keeps the cells at 37°C with 100% humidity. Cell media is supplemented with HEPES in order to maintain pH in the absence of CO_2. The oscillating magnetic field is generated via 4 solenoids positioned around and slightly above the microfluidic device (Figure S2). All solenoids are driven by an alternating current with frequency of 15Hz; two solenoids are driven 90° out of phase. Suspended cells rotate with a frequency of 0.1Hz.

4.2.8 Image Processing

Raw images consist of a grid of cells at regular intervals (each cell is sitting in regularly-spaced microwells). Each live, single cell is cropped from the original image into separate, smaller images, each consisting of a single cell. It is these cropped images of single cells that are analyzed. The basis for measuring cell morphology relies on the accurate delineation of a cell's contours. This task is performed by a pipeline with the image analysis software CellProfiler [**morpho30**]. Once cells are delineated, CellProfiler measures and records the value of different morphological

parameters, such as cell area, perimeter, extent, etc., as well as Zernike moments and Haralick features. For a single experimental run, over 1000 individual cells are processed, and each cell has over 100 measured features.

4.2.9 Computation

All methods described (PCA, SVM, k-NN, Random Forests, AdaBoost, cross validation, grid search) were trained on normalized data (mean 0, standard deviation 1). Implementations were taken from the Scikit package suite, and used without any further modification. All hyperparameters tuned are listed in Table 4.1. Training was performed on a personal laptop.

4.3 Results

Figure 4.4 shows an image of an empty microfluidic device juxtaposed with fluorescence images of cells loaded into the device. As the triangular wells are clearly deliminated, we can be confident in the device's ability to capture cells. The uncropped, loaded cells are presented as an example of a raw data image. Note that most wells contain only a single cell, while some wells contain two or three cells. Any well containing two or more cells is rejected from analysis.

Prior to training a classifier, we use Principal Component Analysis (PCA) to explore and visualize the data. The raw data collected from CellProfiler consists of over 100 measured variables, making data visualization a challenge. With so many measured parameters, it is difficult to select a subset that allows us to visualize the data well. We would like to select a subset that separated the data points well, i.e. maximizes the variance in the data. In essence, PCA is a dimensionality reduction technique. Operationally, in PCA, the data is normalized and the covariance matrix of the data is calculated against itself. The principal components are calculated as

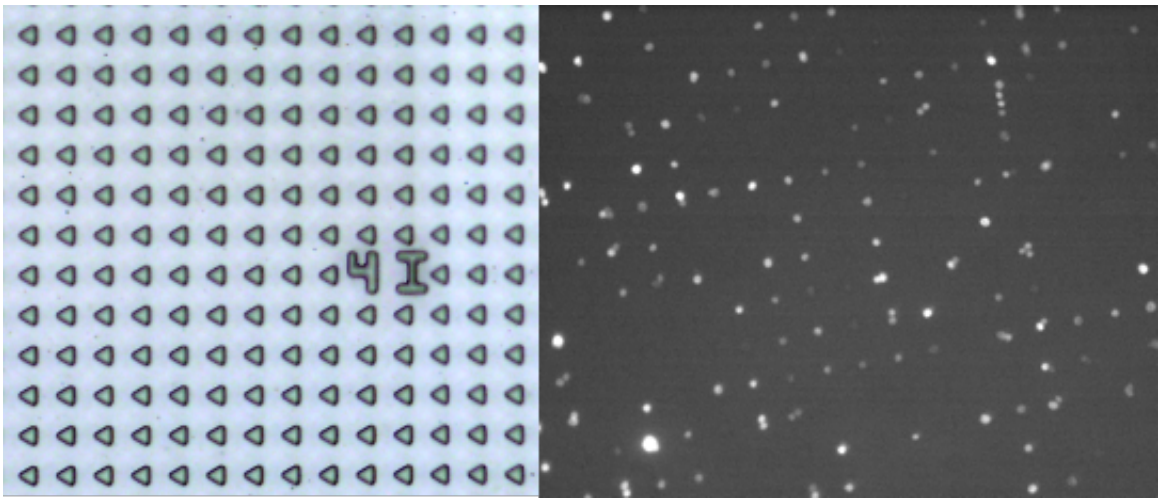

Figure 4.4: Left) A brightfield image of an empty microfluidic device. The triangular wells are well-defined and regular, with side of length 40μm. Right) A fluorescence image of GFP-expressing cells that have been loaded into the microfluidic device.

the eigenvectors and eigenvalues of this covariance matrix. The eigenvectors point in the directions of maximum variance, and the eigenvalues represent the relative magnitude of explained variance in each direction. We can then project our original data onto the princiapl component space,a nd thus visualize a graph of the data where each axes maximizes the variance of the data. Figure 4.5 shows the results of projecting the raw data onto these principal components.

It is always the case that the greatest proportion of the variance is explained by the first principal component. Figure 4.6 shows a modified scree plot, where the x-axis is the nth component, and the y-axis shows the relative proportion of variance explained by that component. Here, the first component explains 97% of the overall variance with the second component explaining 2% overall. The remaining components individually explain a negligible proportion of the total variance. Principal components are linear combinations of the individual parameters. Thus, their interpretation can be challenging. By looking at the individual loadings of each component, we can learn how strongly a given variable contributed to and correlated

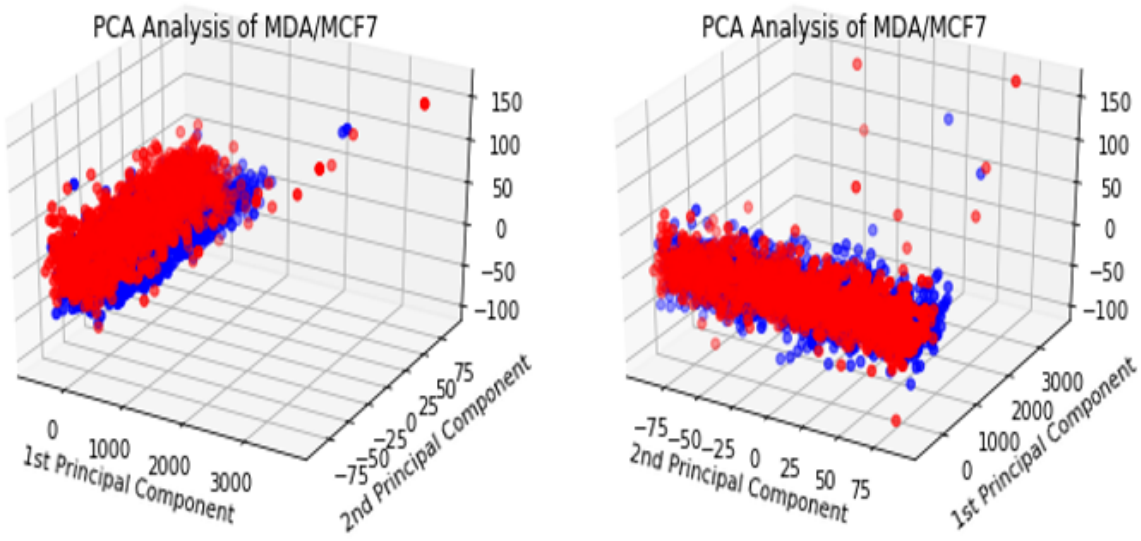

Figure 4.5: Projection of the processed cell image data onto its first three principal components. The same plot is provided with the axis switch to provide different viewing angles. 97% of the variance is explained by the first principal component.

Figure 4.6: A modified scree plot. It shows the relative variance explained by the first 10 principal components. The first component dominates, with 97% of the variance.

with a given component. For both the first and second component, the loadings were dominated by a single variable: *area* and *orientation*, respectively. In their respective components, the loadings for these two variables were at least an order of magnitude larger than the second largest contributor.

Orientation, in this context, is defined as the x-axis of the cropped image and the major length axis of the object (cell). As the cells are rotating in an oscillating magnetic field, the orientation of the cell is liable to change upon additional rounds of imaging. Thus, it seems unlikely that orientation represents a manifestation of a biological condition. Cell area, however,has a simple biological interpretation: the cell size or diameter. As we are comparing two genetically distinct cell lines, it is reasonable to expect that the mean diameter between the two populations is different, as has been reported [159, 128, 119].

While principal component analysis helps with data visualization, and can be employed in classification problems, it inevitably does remove some of the information present in a data set. Thus, we chose to return to the original, normalized data to develop a supervised classifier for identifying the cells. To find a suitable classifier, a grid search approach was employed. Also known as hyperparamter tuning, grid search allows us to test the performance of learning algorithms under different initial conditions. For example, we can compare k-Nearest Neighbor's performance with different values of k. In addition to grid search, we also conducted cross validation. In cross validation, a given classifier and hyperparameter set are tested and trained on multiple different samples of the population. This approach ensures that our results are robust and helps avoid over-fitting.

Table 4.1 shows the best performance results of four classifiers after grid search. Strictly, the random forest algorithm performed best, correctly identify the cells

Table 4.1: Summary of coarse classifier optimization. Tuned hyperparameters are listed as well as the classifier's mean performance with the best hyperparameters obtained. Standard deviation of classifier performance is obtained from threefold cross validation.

Classifier	Hyperparameter(s)	Performance (%)	Standard Deviation
Support Vector Machine	Kernel; regularization	86.5	1.3
Random Forest	Estimators	86.9	2.0
AdaBoost	Estimators; Learning Rate	83.9	1.0
k-Nearest Neighbors	Neighbors	80.8	2.5

Table 4.2: Analysis of the in-class performance using the best tuned hyperparameters obtained from grid search.

Classifier	Hyperparameter(s)	MCF7 (%)	MDA-MB-231 (%)
Support Vector Machine	Kernel= radial; C=1	87.1	85.8
Random Forest	Estimators=500	86.4	87.4
AdaBoost	Estimators=100; Learning Rate=0.5	83.4	84.5
k-Nearest Neighbors	Neighbors=60	81.0	80.6

as 'MDA' or 'MCF-7' 86.9% of time time. However, its performance was within error of the support vector machine, so those two algorithms performed comparably. Adaboost, which is an ensemble method like random forest, performed slightly worse. Finally, k-nearest neighbors had the poorest performance on the data set.

Since the aggregate accuracy of these classifiers can be misleading, Table 4.2 shows the individual classification accuracy of the four classifier's with the best performing hyperparameters yielded form grid search. One might note that the ensemble classes were able to better identify MDA-MB-231 cells while nearest neighbors and the support vector machine performed better on the MCF-7 cells. However, no significant performance differences arose in identifying the two cellular subclasses.

Finally, to gain some understanding of how the classifiers are learning, we performed an ablation study. In this approach, the classification is done on the data set while iteratively removing a single parameter from the training data. By finding the poorest performing classifier, we can determine the "moat significant feature" in the data set, and gain some intuition for which parameters are the most important for

Table 4.3: A summary of results from the ablation study. For each classifier, the worst performance when the most significant parameter is removed from the data set. Analysis of the average score (n=114 parameters) suggests that each parameter contributes only a small amount to the classification.

Classifier	Most Significant Feature	Minimum Score (%)	Average Score (%)
Support Vector Machine	Cell Center X	85.6	86.4
Random Forest	8th Radial Distribution	85.3	86.4
AdaBoost	8th Radial Distribution	81.4	83.6
k-Nearest Neighbors	Entropic Information Measure	80.2	80.7

classification. Table 4.3 shows the results ablation and training of the classifiers.

The ablation study suggests that no feature is particularly critical to the classification algorithms. Table **??** shows the worst performance accuracy found in the abalation study (the worst classification accuracy corresponds to the most significant feature). In each case, removal of the most significant feature had little impact on the overall classification accuracy. The worst performing classifiers were all within 1% of the average classification error, except adaboost. Both ensemble methods found the "8th Radial Distribution" to be the most significant feature, which suggests. However, as the classification performance varied very little by removing individual features, the ablation study suggests that no individual parameter is critical for learning and classification to take place.

4.4 Discussion

While the devices produced by Park have been reproduced, there remain several improvements that could be pursued. During manufacture, precise and even deposition of PDMS-release remains a challenge. Uneven distribution of release agent produces microfluidic devices with damaged or missing canals. Simultaneously, molds without proper release agent deposition become irreparably damaged quickly. Regarding the devices themselves, notably, cured PDMS is practically transparent, but the devices produced as described here suffer from clouding in buffered storage so-

lutions, which render the devices translucent to opaque. This clouding significantly interferes with data collection. The reason for the clouding is unclear. It cannot be attributed to Pluronic F68 or buffer salts in the storage medium, as removing either of these components had no effect on the problem. Incomplete curing is also unlikely to be the source, as the effect is independent of light exposure to the devices. Fortunately, the clouding can be reversed by drying the device overnight, but this presents the hazard of the internal canal drying out.

PCA was performed on a small data set consisting of MDA ad MCF7 cells. The first principal component was able to explain 97% of the variance. As this component was dominated by the *Cell_Area* loading, it is natural to interpret that a great deal of the variance is attributable to that parameter. However, Figure 4.5 shows that the size variance is not polarizing, but exists spread between the two populations. Thus, size alone is not a reliable way to identify between these two cell lines. Indeed, their is significant variation in the literature regarding the mean cell diameter of these lines [159, 128, 119].

It is of significant interest to identify phenotypes and sub-phenotypes of cells robustly without costly genetic or proteomic profiling. Morphodynamics combines several techniques and approaches to permit the classification and clustering of cells. In previous analyses, this technique has been used to classify cells of different genotypes, cells of different phenotypes, and was shown to serve as a suitable Proxy for a Boyden chamber assay [109]. Here, several supervised classifiers have been trained on a small data set. A coarse grid search was performed to find hyperparameters better than defaults, but no extensive optimization has been performed. Three-fold cross validation was used to verify the robustness of the results and avoid problems associated with overfitting. Ultimately, it was found that a random forest classifier

was best able to classify the data. No significant performance difference was found in identifying the two subclasses. An ablation study was performed and determined that no individual parameter was critical for the learning algorithms to classify the cells accurately. Instead, the approach the of using a wide variety of physical and optical features allows us to capture the information necessary to robustly classify the cells. These algorithms were trained on relatively small data sets (approximately 3000 cells), and it is likely true that their performance could be improved with additional data. These results offer a proof of principal that morphodynamics can be used to identify cells using morphology alone, and offers a robust, reliable way to identify cells and could be of significant diagnostic benefit.

CHAPTER V

Summary and Future Directions

5.1 Summary

In this work, we sought to develop technologies that could inform clinicians. The first focus was on developing a reliable, robust potassium sensor. We chose to utilize an ionophore-based sensor for their exquisite selectivity and diverse fabrication methods. We wanted to improve on previous fluorescent potassium sensors by ensuring that quantitative potassium measurements could be taken both in diverse imaging modalities. For fluorescence, this goal was achieved through these use of a reference dye, which allowed for the ratiometric imaging. The sensor was not limited to fluorescence, however, as fluorescence is ill-suited toward *in vivo* measurement. We also performed photoacoustic calibrations, and were able to show *in vitro* that photoacoustic images could be generated that can carry the information of potassium concentration.

This photoacoustic approach was then modified and extended to allow for easier *in vivo* imaging. The inherent pH-cross sensitivity of the sensor was removed by replacing the pH dye with a solvatochromic dye. As the sensor was no longer dependent on the concentrations of protons in the solution, we no longer had to control for pH in our measurements. We were able to perform quantitative, *in vivo* measurements

of potassium. We have shown that the the potassium concentration in the TME is elevated, and determined the potassium concentration to be to 29mM. These results were validated by ICP-MS measurement of the TME fluid's potassium content, and reasonable agreement (r^2=0.70, m=1) was found between the two methods.

In the final chapter, the relationship between a cell's morphology and phenotype is explored. Currently, to determine the phenotype of cell, expensive genetic profiling or antibody techniques are required. We sought to eliminate the need for highly specific biomarkers by correlating a cell's morphology to its phenotypic behavior. This goal was accomplished by loading magnetically-activated cells into a microfluidic device. This device was then placed into an oscillating magnetic field and fluorescence images of the cells were gathered. Upon delineating these images and measuring a variety of physical features, the cells were identified by a machine learning classifier. This method was tested on two genetically distinct populations of breast cancer: MDA-MB-231 and MCF-7 cells. An random forest classifier was trained on the data, and able to accurately identify cells 86.9% of the time with three-fold cross validation.

5.2 Future Directions: Potassium Sensing

Photoacoustic Chemical Imaging of potassium is an attractive goal. Many biological questions, such as the rate of potassium accumulation, its distribution, and the inhibitory dose of potassium remain unanswered. The largest obstacle moving forward is the toxicity of the SDKNP, as its interference with measurement is difficult to predict and it prevents intravenous injection of the nanoparticles. The source of this toxicity is almost assuredly the potassium ionophore, valinomycin. Valinomycin is a well-characterized apoptotic agent. To eliminate this toxicity, valinomycin must be replaced with a less toxic ionophore, such as BME-44. Exploring alternative car-

riers to permit valinomycin replacement with BME-44 is the most direct method of reducing SDKNP's toxicity.

Replacement of BME-44 in the Pluronic F127 SDKNP formulation results in reduced sensor response (data now shown). The reduction in sensitivity is attributed to incomplete solvation and encapsulation of BME-44 in the Pluronic F127 micelle. The long akyl chain in BME-44 may render it relatively liophillic compared to valinomycin. BME-44 has been used for potassium sensing in mixed micelles of Pluronic F68 and P123. The additional polypropylene blocks in P123 may help to better solubilize BME-44. Alternatively, non-Pluronic carriers could be explored. Polyvinyl chloride is frequently employed in the construction of both standard electrodes as well as nanosensors. Further, phospholipid micelles make an attractive choice due to the relative ease of preparation, small radius, and ability to mimic biological structures.

The acute toxicity of the SDKNP prevented its intravenous direction. While solving the toxicity would also likely permit the SDKNP to be administered intravenously, its retention in the TME could be improved by modifying the hydroxyl groups at the ends of the Pluronic polymers. By converting these groups into primary amines, active targeting could be added to the SDKNP, such as the F3 peptide which targets neovasculature. Active targeting increases retention time in the tumor area, and thus would be of significant benefit to the analysis of tumor hyperkalemia.

Finally, the sensitivity of the SDKNP could be adjusted. Optimization of the relative ratios of sensing components has been performed, and our best results reported here. However, the dynamic range of the sensor could be adjusted by modifying the lipophilicity of the solvatochromic dye. Currently, the SDKNP is best suited for small concentrations, approximately 0-20mM. By rendering the solvatochromic dye more hydrophobic, it would take an increasingly large concentration of potassium to

permit a chelation event. By shifting the dynamic range so that the greatest sensitivity is observed from 5-50mM, more precise measurements could be taken using the same approach.

5.3 Future Directions: Morphodynamics

Previously, morphodynamic analysis has been shown to separate cells from a number of phenomenological classes. As shown here, MDA-MB-231 and MCF-7 breast cancer cells were identified and classified. These two cells lines represent 'mesenchymal' and 'epithelial' cell types, respectively. Morphodynamics was further applied to PC3 and HR14 cell lines, which contained the same genotype but differed vastly in their phenotype. Finally, MDA-MB-231 cells that migrated through a Boyden chamber were separated from a control population of MDA cells. These results suggest that morphodynamics is capable of delineating among cell phenotypes without the need for specific biomarkers.

To improve these results, the morphodynamic analysis must be associated with relevant biological data. While delineating two behaviorally distinct cell lines is significant, it will be of great interest to determine the expression profiles of morphodynamically identified populations differ. These expression profiles could take the form of gene sequencing, RNA sequencing, or protein expression profiles. However, it is a significant challenge to gather genetic data about single cells after they have been analyzed via morphodynamics. To move forward, splitting populations prior to training (50% of cells for morphodynamics, 50% of cells for genetic profiling) may offer a starting point. Alternatively, anti-body labeling of cell populations may also be of significant benefit as a 'gold standard'. For the case of epithelial versus mesenchymal cells, the use of a fluorescent EpCAM anti-body could be used

to demonstrate the expression of epithelial cell adhesion molecules in epithelial cells that should be absent in the mesenchymal cell line. This experiment would allow fundamental expression patterns to be linked to the morphodynamic analysis.

From an experimental stand point, morphodynamics could be improved by gathering additional information, particularly about the cell nucleus. A simple cell stain, such as DAPI, could allow for morphological information about cell nuclei to be gathered along with whole-cell morphologies. In addition, further optimization of the classifiers could be done. Alternatively, other approaches could be adopted, such as neural networks or, as previously done, unsupervised learning algorithms. While unsupervised learning algorithms have the advantage of making no inherent assumptions about the underlying biological data, the results of such analyses are difficult to interpret without additional biological data. Identified subphenotypes may be attributed to noise, variations in the cell cycle, or true morphological manifestations of cell phenotypes. Further testing would be required to confirm these results.

Bibliography

[1] Abbott A. "Cell culture: Biology's new dimension". In: *Nature* 424 (2003), pp. 870–872.

[2] Armulik A, Genove G, and Betsholtz C. "Pericytes: developmental, physiological, and pathological perspectives, problems, and promises." In: *Developmental Cell* 21 (2011), pp. 193–215.

[3] Bauer A et al. "Quantitative photoacoustic imaging: correcting for heterogeneous light fluence distributions using diffuse optical tomography." In: *Journal of Biomedical Optics* 16 (2011), p. 096016.

[4] Pasqualato A et al. "Quantitative Shape Analysis of Chemoresistant Colon Cancer Cells: Correlation between Morphotype and Phenotype". In: *Experimental Cell Research* 7 (2012), pp. 835–846.

[5] Pasqualato A et al. "Shape in Migration". In: *Cell Adhesion and Migration* 5 (2013), pp. 450–459.

[6] Pitto-Barry A and Barry NPE. "Pluronic block copolymers in medicine: from chemical and biological versatility to rationalisation and clinical advances". In: *Polymer Chemistry* 5 (2014), pp. 3291–3297.

[7] Ray A et al. "Lifetime-based photoacoustic oxygen sensing in vivo". In: *Journal of Biomedical Optics* 17 (2012).

[8] Ray A et al. "Sonophoric nanoprobe aided pH measurement in vivo using photoacoustic spectroscopy". In: *Analyst* 138 (2013), pp. 3126–3130.

[9] Sigel A, Sigel H, and Sigel RK. "Interrelations between essential metal ions and human diseases." In: *Springer* ().

[10] Wouters A et al. "Review: Implications of In Vitro Research on the Effect of Radiotherapy and Chemotherapy Under Hypoxic Conditions". In: *The Oncologist* 12 (2007), pp. 690–712.

[11] Cohen AA et al. "Dynamic Proteomics of Individual Cancer Cells in Response to a Drug". In: *Science* 322 (2008), pp. 1511–1516.

[12] Baker AF et al. "Identification of Thioredoxin Interacting Protein 1 as a Hypoxia-Inducible Factor 1 Induced Gene in Pancreatic Cancer". In: *Pancreas* 36 (2008).

[13] Watts AS et al. "Centrifugal Microfluidics with Integrated Sensing Microdome Optodes for Multiion Detection". In: *Analytical Chemistry* 79 (2007), pp. 8046–8054.

[14] Cox B et al. "Quantitative spectroscopic photoacoustic imaging: a review". In: *Journal of Biomedical Optics* 17 (2012), p. 061202.

[15] Teicher BA, Lazo JS, and Srtorelli AC. "Classification of Antineoplastic Agents by their Selective Toxicities toward Oxygenated and Hypoxic Tumor Cells". In: *Cancer Research* 41 (1981), p. 73.

[16] Teicher BA et al. "Classification of antineoplastic treatments by their differential toxicity toward putative oxygenated and hypoxic tumor subpopulations in vivo in the FSaIIC murine fibrosarcoma". In: *Cancer Research* 50 (1990), pp. 3339–3344.

[17] Bakal C et al. “Quantitative Morphological Signatures Define Local Signaling Networks Regulating Cell Morphology”. In: *Science* 316 (2007), pp. 1753–1756.

[18] Bortner CD, Hughes FM, and Cidlowski JA. “A Primary Role for K and Na Efflux in the Activation of Apoptosis”. In: *Journal of Biological Chemistry* 272 (1997).

[19] Meacham CE and Morrison SJ. “Tumour heterogeneity and cancer cell plasticity”. In: *Nature* 501 (2013), pp. 328–337.

[20] Lee CH et al. “Chemical Imaging in Vivo: Photoacoustic-Based 4-Dimensional Chemical Analysis”. In: *Analytical Chemistry* 91 (2019), pp. 2561–2569.

[21] Hanahan D and Weinberg RA. “Hallmarks of cancer: the next generation”. In: *Cell* 144 (2011), pp. 646–674.

[22] Si D et al. “Nanoparticle PEBBLE Sensors for Quantitative Nanomolar Imaging of Intracellular Free Calcium Ions”. In: *Analytical Chemistry* 84 (2012), pp. 978–986.

[23] McDonald DM, Thurston G, and Baluk P. “Endothelial gaps as sites for plasma leakage in inflammation”. In: *Microcriculation* 6 (1999), pp. 7–22.

[24] Dibrova DV et al. “Ancient Systems of Sodium/Potassium Homeostasis as Predecessors of Membrane Bioenergetics”. In: *Biochemistry* 80 (2015), pp. 495–516.

[25] Alizadeh E et al. “Measuring Systematic Changes in Invasive Cancer Cell Shape Using Zernike Moments”. In: *Integrative Biology* 8 (2016), pp. 1183–1193.

[26] Bakker E, Buhlmann P, and Pretsch E. “Carrier-Based Ion-Selective Electrodes and Bulk Optodes. 1. General Characteristics”. In: *Chemical Reviews* 97 (1997), pp. 3083–3132.

[27] Bakker E, Buhlmann P, and Pretsch E. “Carrier-Based Ion-Selective Electrodes and Bulk Optodes. 2. Ionophores for Potentiometric and Optical Sensors”. In: *Chemical Reviews* 98 (1998), pp. 1593–1688.

[28] Mercep E, Dean-Ben X, and Razanksy D. “Imaging of blood flow and oxygen state with a multi-segment optoacoustic ultrasound array”. In: *Photoacoustics* 10 (2018), pp. 48–53.

[29] R Eil et al. “Ionic immune suppression within the tumor microenvironment limits T cell effector function”. In: *Nature* 537 (2016), pp. 539–543.

[30] Park EJ et al. “Ratiometric optical PEBBLE nanosensors for real-time magnesium ion concentrations inside viable cells.” In: *Analytical Chemistry* 75 (2003), pp. 3784–3791.

[31] Danhier F, Feron O, and Preat V. “To exploit the tumor microenvironment: passive and active tumour targeting of nanocarriers for anti-cancer drug delivery”. In: *Journal of Controlled Release* 148 (2010), pp. 135–146.

[32] S Feske. “PRAI1 and STIM1 deficiency in human and mice: roles of store-operated Ca2+ entry in the immune system and beyond”. In: *Immunology Reviews* 231 (2009), pp. 189–209.

[33] Lahav G et al. “Dynamics of the p53-Mdm2 feedback loop in individual cells”. In: *Nature Genetics* 36 (2004), pp. 147–150.

[34] Mistlberger G, Crespo GA, and Bakker E. “Ionophore-Based Optical Sensors”. In: *Annual Reviews of Analytical Chemistry* 7 (2014), pp. 483–512.

[35] Nie G et al. “Hydrogel nanoparticles with covalently linked coomassie blue for brain tumor delineation visible to the surgeon.” In: *Small* 26 (2012), pp. 884–891.

[36] L Gattinoni et al. “A human memory T cell subset with stem cell-like properties”. In: *Nature Medicine* 17 (2011), pp. 1290–1297.

[37] L Gattinoni et al. “Wnt signalling arrests effector T cell diffrentian and generates CD8+ memory stem cells”. In: *Nature Medicine* 15 (2009), pp. 808–813.

[38] Alderton GK. “Microenvironment: an exercise in restraint”. In: *Nature Reviews Cancer* 17 (2014), pp. 2205–2218.

[39] Luke GP, Nam SY, and Emelianov SY. "Optical wavelength selection for improved spectroscopic photoacoustic imaging". In: *Photoacoustics* 1 (2013), pp. 36–42.

[40] Clark H et al. "Optical nanosensors for chemical analysis inside single living cells. 1. Fabrication, characterization, and methods for intracellular delivery of PEBBLE sensors." In: *Analytical Chemistry* 71 (1999), pp. 4831–4836.

[41] Meng H et al. "Two-wave nanotherapy to target the stroma and optimize gemeitabine delivery to a human pancreatic cancer model in mice". In: *ACS Nano* 7 (2013), pp. 10048–10065.

[42] Nishihara H. "Human pathological basis of blood vessels and stromal tissue for nanotechnology". In: *Advanced Drug Delivery Reviews* 74 (2014), pp. 19–27.

[43] Wiig H, Aukland K, and Tenstad O. "Isolation of interstitial fluid from rat mammary tumors by a centrifugation method". In: *American Journal of Physiology - Heart and Circulatory Physiology* 284 (2003).

[44] H Haslene-Hox et al. "A new method for isolation of interstitial fluid from human solid tumors applied to proteomic analysis of overian carcinoma tissue". In: *PLos ONE* 6 (2011).

[45] PC Ho et al. "Phosphoenolpyruvate is a metabolic checkpoint of anti-tumor T cell responses". In: *Cell* 162 (2015), pp. 1217–1228.

[46] Koronczi I et al. "Development of a submicron optochemical potassium sensor with enhanced stability due to internal reference". In: *Sensors and Actuators B* 51 (1998), pp. 188–195.

[47] Mellman I, Coukos G, and Dranoff F. "Cancer immunotherapy comes of age". In: *Nature* 480 (2011).

[48] Tsagkatakis I, Peper S, and Bakker E. "Spatial and spectral imaging of single micrometer-sized solvent cast fluorescent plasticized poly(-vinyl chloride) sensing particles". In: *Analytical Chemistry* 73 (2001), pp. 315–320.

[49] Elabyad IA et al. "First In Vivo Potassium-39 (39K) MRI at 9.4 T Using Conventional Copper Radio Frequency Surface Coil Cooled to 77 K". In: *IEEE Transactions on Biomedical Engineering* 61 (2014), pp. 334–345.

[50] Tannock IF and Rotin D. "Acid pH in tumors and its potential for therapeutic exploitation". In: *Cancer Research* 49 (1989), pp. 4373–4384.

[51] Jo J et al. "In Vivo Photoacoustic Lifetime Based Oxygen Imaging with Tumor Targeted G2 Polyacrylamide Nanosonophores". In: *ACS Nano* 13 (2019), pp. 14024–14032.

[52] Jo J et al. "In vivo quantitative imaging of tumor pH by nanosonophore assisted multispectral photoacoustic imaging". In: *Nature Communications* 8 (2017).

[53] Kosla J et al. "Metastasis of aggressive amoeboid sarcoma cells is dependent on Rho/ROCK/MLC signaling". In: *Cell Communication and Signaling* 11 (2013).

[54] Laufer J et al. "Quantitative spatially resolved measurement of tissue chromophore concentrations using photoacoustic spectroscopy: application to the measurement of blood oxygenation and haemoglobin concentration." In: *Physics in Medicine and Biology* 52 (2007), pp. 141–168.

[55] Wike-Hooley JL, Haveman J, and Reinhold HS. "The relevance of tumour pH to the treatment of malignant disease". In: *Radiotherapy and Oncology* 2 (1984), pp. 343–366.

[56] Dubach JM, Harjes DI, and Clark HA. "Fluorescent Ion-Selective Nanosensors for Intracellular Analysis with Improved Lifetime and Size". In: *Nano Letters* 7 (2007), pp. 1827–1831.

[57] Dubacj JM et al. "FVisualizing sodium dynamics in isolated cardiomyocytes using fluorescent nanosensors". In: *Proceedings of the National Academy of Sciences* 106 (2009), pp. 16145–16150.

[58] Sumner JP and Kopelman R. "Alexa Fluor 488 as an iron sensing molecule and its application in PEBBLE nanosensors". In: *Analyst* 130 (2005), pp. 528–533.

[59] Sumner JP et al. "A fluorescent PEBBLE nanosensor for intracellular free zinc". In: *Analyst* 127 (2002), pp. 11–16.

[60] Park JY et al. "Single cell trapping in larger microwells capable of supporting cell spreading and proliferation". In: *Nanofluidics* 8 (2009), pp. 263–268.

[61] Cash K et al. "Optical Drug Monitoring: Photoacoustic Imaging of Nanosensors to Monitor Therapeutic Lithium In Vivo". In: *ACS Nano* 9 (2016), pp. 1692–1698.

[62] Daoudi K et al. "Correcting photoacoustic signals for fluence variations using acousto-optic modulation". In: *Optics Express* 20 (2012), pp. 14117–14129.

[63] Graham K and Unger E. "Overcoming tumor hypoxia as a barrier to radiotherapy, chemotherapy and immunotherapy in cancer treatment". In: *International Journal of Nanomedicine* 13 (2018), pp. 6049–6058.

[64] Hosaka K et al. "Tumour PDGF-BB expression levels determine dual effects of anti-PDGF drugs on vascular remodelling and metastasis". In: *Nature Communications* 4 (2013).

[65] Maslov K, Zhang HF, and Wang LV. "Effects of wavelength-dependent fluence attenuation on the noninvasive photoacoustic imaging of hemoglobin oxygen saturation in subcutaneous vasculaturein vivo". In: *Inverse Problems* 23 (2007), S113–S122.

[66] Wygladacz K and Bakker E. "Imaging fiber microarray fluorescent ion sensors based on bulk optode microspheres". In: *Analytica Chimica Acta* 532 (2004), pp. 61–69.

[67] Yokoi K et al. "Capillary-wall collagen as a biophysical marker of nanotherapeutic permeability into the tumor microenvironment". In: *Cancer Research* 74 (2014), pp. 4239–4246.

[68] Baumann KN et al. "An active DNA-based nanoprobe for photoacoustic pH imaging". In: *Chemical Communications* 54 (2018), p. 10176.

[69] Alfarouk KO et al. "Glycolysis, tumor metabolism, cancer growth and dissemination. A new pH-based etiopathogenic perspective and therapeutic approach to an old cancer question". In: *Oncoscience* 1 (2014), pp. 777–802.

[70] Miao L and Huang L. "Exploring the Tumor Microenvironment with Nanoparticles". In: *Cancer Treatment Research* 166 (2015), pp. 193–226.

[71] Zhang L, Nishihara H, and Kano MR. "Pericyte-coverage of human tumor vasculature and nanoparticle permeability". In: *Biological and Pharmaceutical Bulletin* 35 (2012), pp. 761–766.

[72] Harrison LB et al. "Impact of tumor hypoxia and anemia on radiation therapy outcomes". In: *The Oncologist* 7 (2002), pp. 492–508.

[73] Gerweck LE, Vijayappa S, and Kozin S. "Tumor pH controls the in vivo efficacy of weak acid and base chemotherapeutics". In: *Molecular Cancer Therapeutics* 5 (2006), pp. 1275–1279.

[74] Augath M et al. "In vivo 39K, 23Na and 1H MR imaging using a triple resonant RF coil setup". In: *Journal of Magnetic Resonance* 200 (2009), pp. 134–136.

[75] Bamsey M, Berinstain A, and Dixon M. "Development of a potassium selective optode for hydroponic nutrient solution monitoring". In: *Analytica Chimica Acta* 737 (2012), pp. 72–82.

[76] Brasuel M et al. "Fluorescent Nanosensors for Intracellular Chemical Analysis: Decyl Methacrylate Liquid Polymer MAtrix and Ion-Exchange-Based Potassium PEBBLE Sensors with Real-Time Application to Viable Rat C6 Glioma Cells". In: *Analytical Chemistry* 73 (2001), pp. 2221–2228.

[77] Brasuel M et al. "Ion concentrations in live cells from highly selective ion correlation fluorescent nano-sensors for sodium". In: *Proceedings of IEEE Sensors* 281 (2002), pp. 288–292.

[78] Egebald M, Rasch MG, and Weaver VM. "Dynamic interplay between the collagen scaffold and tumor evolution". In: *Current Opinion in Cell Biology* 2 (2010), pp. 697–706.

[79] Furuhasi M et al. "Platelet-derived growth factor production by B16 melanoma cells leads to increased pericye abundance in tumors and an associated increase in tumor growth rate". In: *Cancer Research* 64 (2004), pp. 2725–2733.

[80] Hockel M and Vaupel P. "Tumor Hypoxia: Definitions and Current Clinical, Biologic, and Molecular Aspects". In: *Current Opinion in Pharmacology* 93 (2001), pp. 266–276.

[81] Kanapathipillai M, Brock A, and Ingber DE. "Nanoparticle targeting of anti-cancer drugs that alter intracellular signaling or influence the tumor microenvironment". In: *Advanced Drug Delivery Reviews* (2014).

[82] Shortreed M, Bakker E, and Kopelman R. "Miniature Sodium-Selective Ion-Exchange Optode with Fluorescent pH Chromoionophores and Tunable Dynamic Range". In: *Analytical Chemistry* 68 (1996), pp. 2656–2662.

[83] Jacobetz MA et al. "Hyaluronan imparis vascular function and drug delivery ina mouse model of pancreatic cancer". In: *Gut* 62 (2013), pp. 112–120.

[84] Swartz MA and Lund AW. "Lymphatic and interstitial flow in the tumor microenvironment: linking mechanobiology with immunity". In: *Nature Reviews Cancer* 12 (2012), pp. 210–219.

[85] I Mellman, G Coukos, and G Dranoff. "Cancer immunotherapy comes of age". In: *Nature* 480 (2011), pp. 480–489.

[86] Brasuel MG et al. "Liquid polymer nano-PEBBLEs for Cl- analysis and biological applications". In: *Analyst* 128 (2003), pp. 1262–1267.

[87] AE Mirrakhimov et al. "Tumor lysis syndrome in solid tumors: an up to date review of the literature". In: *Rare Tumors* 6 (2014), pp. 68–76.

[88] Mitchell MJ and King MR. "Computational and experimental models of cancer cell response to fluid shear stress". In: *Frontiers of Oncology* 3 (2013).

[89] Danquah Mk, Zhang XA, and Mahato RI. "Extravasation of polymeric nanomedicines across tumor vasculature". In: *Advanced Drug Delivery Reviews* 63 (2011), pp. 623–639.

[90] Horsman MR et al. "Imaging hypoxia to improve radiotherapy outcome". In: *Nature Reviews Clinical Oncology* 9 (2012), pp. 674–687.

[91] Kano MR et al. "Comparison of the effects of the kinase inhibitors imatinib, sorafenib, and transforming growth factor-beta receptor inhibitor on extravasation of nanoparticles from neovasculature". In: *Cancer Science* 100 (2009), pp. 173–180.

[92] Mancuso MR et al. "Rapid vascular regrowth in tumors after reversal of VEGF inhibition". In: *Journal of Clinical Investigation* 116 (2006), pp. 2610–2621.

[93] Shortreed MR, Dourado S, and Kopelman R. "Development of a fluorescent optical potassium-selective ion sensor with ratiometric response for intracellular applications". In: *Sensors and Actuators B: Chemical* 38 (1997), pp. 8–12.

[94] Reddy GR Bhojani MS et al. "Vascular Targeted Nanoparticles for Imaging and Treatment of Brain Tumors". In: *Clinical Cancer Research* 12 (2006), p. 6677.

[95] Arabul MU et al. "Imaging of blood flow and oxygen state with a multi-segment optoacoustic ultrasound array". In: *Photoacoustics* 15 (2019), p. 100140.

[96] Sitkovsky MV et al. "Hostile, hypoxia A2-adenosinergic tumor biology as the next barrier to overcome for tumor immunologists". In: *Cancer Immunology Research* 2 (2014), pp. 598–605.

[97] Stuurman N et al. "Computer Control of Microscopes using micromanager". In: *Current Protocols in Molecular Biology* (2010).

[98] Chahine NO et al. "Direct measurement of osmotic pressure of glycosaminoglycan solutions by membrane osmometry at room temperature". In: *Biophysical Journal* 89 (2005), pp. 1543–1550.

[99] Nir O et al. “Inference of RhoGAP/GTPase Regulation Using Single-Cell Morphological Data from a Combinatorial RNAi Screen”. In: *Genome Research* 20 (2010), pp. 372–380.

[100] Tredan O et al. “Drug resistance and the solid tumor microenvironment”. In: *Journal of the National Cancer Institute* 99 (2007), pp. 1441–1554.

[101] Warburg O and Wind F. “The metabolism of tumors in the body”. In: *The Journal of General Physiology* 8 (1927), pp. 519–530.

[102] K Omilusik et al. “The Ca(v) 1.4 calcium channel is a critical regulator of T cell receptor signaling and naive T cell homeostasis”. In: *Immunity* 35 (2011), pp. 349–360.

[103] Baluk P et al. “Abnormalities of basement membrane on blood vessels and endothelial sprouts in tumors”. In: *American Journal of Pathology* 163 (2003), pp. 1801–1805.

[104] Pascual-Vargas P et al. “Inference of RhoGAP/GTPase Regulation Using Single-Cell Morphological Data from a Combinatorial RNAi Screen”. In: *Scientific Data* 4 (2017).

[105] Yurchenco PD and Ruven GC. “Basement membrane structure in situ: evidence for lateral associations in type IV collagen network”. In: *Journal of Cell Biology* 105 (1987), pp. 2559–2568.

[106] Tremblay PL, Huot J, and Auger FA. “Mechanisms by which E-selectin regulates diapedesis of colon cancer cells under flow conditions”. In: *Cancer Research* 68 (2008), pp. 5167–5176.

[107] Shao Q and Ashkenazi S. “Photoacoustic lifetime imaging for direct in vivo tissue oxygen monitoring”. In: *Journal of Biomedical Optics* 20 (2015).

[108] Shao Q et al. “In vivo photoacoustic lifetime imaging of tumor hypoxia in small animals.” In: *Journal of Biomedical Optics* 18 (2013).

[109] Elbez R. “Nanoparticle Induced Cell Magneto-Rotation for the Multiplexed Monitoring of Morphology, Stress and Drug Sensitivity of Suspended Single Cancer Cells”. In: *Thesis; University of Michigan* (2015).

[110] Munoz-Planillo R et al. “K(+) efflux is the common trigger of NLRP3 inflammasome activation by bacterial toxins and particulate matter”. In: *Immunity* 38 (2013), pp. 1142–1153.

[111] Retter R et al. “Flow cytometric ion detection with plasticized poly(vinyl chloride) microspheres containing selective ionophores”. In: *Analytical Chemistry* 74 (2002), pp. 5420–5425.

[112] Retter R et al. “Flow cytometric ion detection with plasticized poly(vinyl chloride) microspheres containing selective lonophores”. In: *Analytical Chemistry* 15 (2002), pp. 5420–5425.

[113] Umathum R, Rosler MB, and Nagel AM. “In Vivo 39K MR Imaging of Human Muscle and Brain”. In: *Radiology* 269 (2013), pp. 569–576.

[114] Johnson RD et al. “Development of a fully integrated analysis system for ions based on ion-selective optodes and centrifugal microfluidics.” In: *Analytical Chemistry* 75 (2001), pp. 3940–3946.

[115] Leone RD, Horton MR, and Powell JD. “Something in the air: hyperoxic conditioning of the tumor microenvironment for enhanced immunotherapy”. In: *Cancer Cell* 27 (2017), pp. 435–436.

[116] Siphanto RI et al. “Serial noninvasive photoacoustic imaging of neovascularization in tumor angiogenesis”. In: *Optics Express* 13 (2005), pp. 89–95.

[117] CH Richards et al. “The prognostic value of histological tumor necrosis in solid organ malignant disease: a systematic review”. In: *Future Oncology* 7 (2011), pp. 1223–1235.

[118] Jain RK and Stylianopuolos T. “Delivering nanomedicine to solid tumors”. In: *Nature Reviews Clinical Oncology* 7 (2000), pp. 653–664.

[119] Rudzka. “Migration through physical constraints is enabled by MAPK-induced cell softening via actin cytoskeleton re-organization”. In: *Lab on a Chip* 12 (2012), pp. 2362–2368.

[120] Inoue S. "Ultrastructure of Basement Membranes". In: *International Review of Cytology* 117 (1989), pp. 57–98.

[121] Ozawa S et al. "Ammonia gas selective optical sensors based on neutral ionophores". In: *Analytical Chemistry* 63 (1991), pp. 640–644.

[122] Pilon-Thomas S et al. "Neutralization of Tumor Acidity Improves Antitumor Responses to Immunotherapy". In: *Cancer Research* 76 (2016), pp. 1381–1390.

[123] Rockwell S et al. "Hypoxia and radiation therapy: past history, ongoing research, and future promise". In: *Current Molecular Medicine* 9 (2009), pp. 442–458.

[124] Strese S et al. "Effects of hypoxia on human cancer cell line chemosensitivity". In: *BMC Cancer* 13 (2013), p. 331.

[125] Tay S et al. "Single-cell NF-kappaB dynamics reveal digital activation and analogue information processing". In: *Nature* 466 (2010), pp. 267–271.

[126] Yang S et al. "Functional imaging of cerebrovascular activities in small animals using high-resolution photoacoustic tomography." In: *Medical Physics* 34 (2007), pp. 3294–3301.

[127] M Sitkovsky and D Lukashev. "Regulation of immune cells by local-tissue oxygen tension: HIF1 alpha and adenosine receptors". In: *Nature Reviews Immunology* 5 (2005), pp. 712–721.

[128] Arya SK et al. "Breast tumor cell detection at single cell resolution using an electrochemical impedance technique." In: *Lab on a Chip* 12 (2012), pp. 2362–2368.

[129] Barker SLR, Thorsrud BA, and Kopelman R. "Nitrite- and Chloride-Selective Fluorescent Nano-Optodes and in Vitro Application to Rat Conceptuses". In: *Analytical Chemistry* 70 (1998), pp. 100–104.

[130] Barker SLR, Shortreed MR, and Kopelman R. "Utilization of Lipophilic Ionic Additives in Liquid Polymer Film Optodes for Selective Anion Activity Measurements". In: *Analytical Chemistry* 69 (1997), pp. 990–995.

[131] Buck SM et al. "Nanoscale probes encapsulated by biologically localized embedding (PEBBLEs) for ion sensing and imaging in live cells." In: *Talanta* 10 (2004), pp. 41–59.

[132] Hatfield SM and Sitkovsky M. "A2A adenosine receptor antagonists to weaken the hypoxia HIF 1 driven immunosuppression and improve immunotherapies of cancer". In: *Current Opinion in Pharmacology* 29 (2016), pp. 90–96.

[133] Lyons SM et al. "Changes in Cell Shape Are Correlated with Metastatic Potential in Murine and Human Osteosarcomas". In: *Biology Open* 5 (2016), pp. 289–299.

[134] Tan SSS et al. "Reversible optical sensing membrane for the determination of chloride in serum". In: *Analytica Chimica Acta* 255 (1991), pp. 35–44.

[135] Ashkenazi S Huang SW et al. "Oxygen sensing for in vivo imaging by photoacoustic lifetime probing". In: (2008).

[136] Stylianopoulos T et al. "Diffusion anisotropy in collagen gels and tumors: the effect of fiber network orientation". In: *Biophysical Journal* 99 (2010), pp. 3119–3128.

[137] Horvath TD et al. "Ratiometric photoacoustic sensing of pH using a "sonophore"". In: *Analyst* 6 (2008).

[138] Padera TP et al. "Pathology: cancer cells compress intratumour vessels". In: *Nature* 427 (2004), p. 695.

[139] E Tran et al. "Cancer immunotherapy based on mutation-specific CD4+ T cells in a patient with epithelial cancer". In: *Science* 344 (2014), pp. 641–645.

[140] Ruckh TT et al. "Ion-Switchable Quantum Dot Förster Resonance Energy Transfer Rates in Ratiometric Potassium Sensors". In: *ACS Nano* 10 (2016), pp. 4020–4030.

[141] Ruckh TT et al. “Polymer-free optode nanosensors for dynamic, reversible, and ratiometric sodium imaging in the physiological range.” In: *Scientific Reports* 3 (2013), p. 3366.

[142] Huber V et al. “Cancer acidity An ultimate frontier of tumor immune escape and a novel target of immunomodulation”. In: *Seminars in Cancer Biology* 43 (2017), pp. 74–89.

[143] SK Vodnala et al. “T cell stemness and dysfunction in tumors are triggered by a common mechanism”. In: *Science* 363 (2019).

[144] Chauhan VP et al. “Normalization of tumour blood vessels improves the delivery of nanomedicines in a size-dependent manner”. In: *Nature Nanotechnology* 7 (2012), pp. 383–388.

[145] Turitto VT. “Blood viscosity, mass transport, and thrombogenesis”. In: *Frontiers of Oncology* 6 (1982), pp. 139–177.

[146] Tan W et al. “Submicrometer intracellular chemical optical fiber sensors”. In: *Science* 258 (1992), pp. 778–781.

[147] LV Wang. “Multiscale photoacoustic microscopy and computed tomography.” In: *Nature Photonics* 3 (2009), pp. 503–509.

[148] Stein WD. “The Sodium Pump in the Evolution of Animal Cells”. In: *Philosophical Transactions: Biological Sciences* 349 (1995), pp. 263–269.

[149] H Wiig et al. “Interstial fluid: the overlooked component of the tumor microenvrionment?” In: *Fibrogenesis* 3 (2010).

[150] Gibbons WS, Patel HM, and Kusy RP. “Effects of plasticizers on the mechanical properties of poly(vinyl chloride) membranes for electrodes and biosensors”. In: *Polymer* 38 (1997), pp. 2633–2642.

[151] Wang X et al. “Noninvasive laser-induced photoacoustic tomography for structural and functional in vivo imaging of the brain”. In: *Nature Biotechnology* 21 (2003), pp. 803–806.

[152] Xie X and Bakker E. “Ion selective optodes: from bulk to the nanoscale”. In: *Analytical and Bioanalytical Chemistry* 407 (2015), pp. 3899–3910.

[153] Xie X, Zhai J, and Bakker E. “Potentiometric Response from Ion-Selective Nanospheres with Voltage-Sensitive Dyes”. In: *Journal of the American Chemical Society* 86 (2014), pp. 2853–2856.

[154] Xie X et al. “Determination of pK(a) Values of Hydrophobic Colorimetric pH Sensitive Probes in Nanospheres.” In: *Analytical Chemistry* 88 (2016), pp. 3015–3018.

[155] Xie X et al. “Ion-Selective Optical Nanosensors Based on Solvatochromic Dyes of Different Lipophilicity: From Bulk Partitioning to Interfacial Accumulation.” In: *ACS Sensors* 1 (2016), pp. 516–520.

[156] Xie X et al. “Potassium-selective optical microsensors based on surface modified polystyrene microspheres”. In: *Chemical Communications* 50 (2014), pp. 4592–4595.

[157] Boucher Y and Jain K. “Microvascular pressure is the principal driving force for interstitial hypertension in solid tumors: implications for vascular collapse”. In: *Cancer Research* 52 (1992), pp. 5110–5114.

[158] Koo Lee Y, Smith R, and Kopelman R. “Nanoparticle PEBBLE Sensors in Live Cells and In Vivo”. In: *Annual Review of Analytical Chemistry* 2 (2009), pp. 57–76.

[159] Liu Z et al. “Microfluidic cytometric analysis of cancer cell transportability and invasiveness”. In: *Scientific Reports* 5 (2015), p. 14272.

[160] Yin Z et al. “A Screen for Morphological Complexity Identifies Regulators of Switch-like Transitions between Discrete Cell Shapes”. In: *Nature Cell Biology* 15 (2013), pp. 860–871.

[161] Zhou Z et al. “Proof of Concept for identifyting cystic fibrosis from perspiration samples”. In: *Proceedings of the National Academy of Sciences* 49 (2019), pp. 24408–24412.

[162] W Zimmerli and JI Gallin. “Pus potassium”. In: *Inflammation* 12 (1988), pp. 37–43.

[163] Ren ZX et al. “Suitable Parameter Choice on Quantitative Morphology of A549 Cell in Epithelial-Mesenchymal Transition”. In: *Bioscience Reports* 35 (2015).